Ring-Moat Dome Structures (RMDSs) in the Lunar Maria: Statistical, Compositional, and Morphological Characterization and Assessment of Theories of Origin

Feng Zhang[1], James W. Head[2], Christian Wöhler[3], Roberto Bugiolacchi[1], Lionel Wilson[4], Alexander T. Basilevsky[5], Arne Grumpe[3], Yong L. Zou[6]

[1]State Key Laboratory of Lunar and Planetary Sciences, Macau University of Science and Technology, Macau, China, [2]Department of Earth, Environmental and Planetary Sciences, Brown University, Providence, RI, 02912 USA, [3]Image Analysis Group, TU Dortmund University, Dortmund, Germany, [4]Lancaster Environment Centre, Lancaster University, Lancaster, UK, [5]Vernadsky Institute of Geochemistry and Analytical Chemistry, Russian Academy of Sciences, Moscow, Russia, [6]National Space Science Center, Chinese Academy of Sciences, Beijing, China

Abstract

Ring-moat dome structures (RMDSs) are positive morphologic features found clustered across many mare regions on the Moon, of which only a few isolated examples have been previously reported. Our continuing survey has expanded the known locations of the RMDSs from ~2600 to over 8,000, indicating that RMDSs are more common geological features than previously thought. This work presents a detailed geomorphological analysis of 532 RMDSs identified in several mare basins. The combination of detailed elemental mapping, morphological and morphometric analyses, spatial distribution relationships with other geologic structures, and comparison with terrestrial analogs lead us to conclude that (1) RMDSs represent low circular mounds with diameters of a few hundred meters (average about 200 m) and a mean height of 3.5 m. The mounds are surrounded by moats ranging from tens to over one hundred meters in width and up to several meters in depth; (2) there is a wide variation of titanium abundances, although RMDSs are more commonly found in mare regions of moderate-to-high titanium content (> 3 wt% TiO_2); (3) RMDSs are found to occur on or around fractures, graben and volcanic edifices (small shields and cones); (4) a spatial association between RMDSs and IMPs (Irregular Mare Patches, see Braden et al., 2014) is observed, suggesting that both may form from related lava flows; (5) comparisons between RMDSs and lava inflationary structures on Earth support an inflation-related extrusive nature and a genetic relationship with host lava flow processes, and (6) RMDS embayment relationships with craters of different degradation ages superposed on the host mare, and regolith development models, produces conflicting age relationships and divide theories of RMDS origin into two categories, 1) synchronous with the emplacement and cooling of the host lava flows ~3-4 Ga, and 2) emplaced substantially after the host mare lava unit, in the period ~0-3 Ga. We outline the evidence supporting this age conundrum and implications for the different theories of origin and describe future research avenues to help resolve these outstanding questions.

Plain Language Summary

The research reported in this paper is focused on the statistical, compositional, and morphological characterization of a newly documented lunar lava flow surface feature characterized by very low, circular- or ellipse-shaped mounds typically several hundred meters across and surrounded by ring depressions. Detailed measurement of 532 mounds shows that their diameters range from 68 to 645 meters, and heights from 0.4 to 14 m. The surrounding ring depressions are tens to more than one hundred meters in width and have depths up to several meters. These mounds have complex relationships with circular and irregular depressions or degraded craters. Compositional mapping results show that this type of mound preferentially forms in lava flow fields of moderate to high titanium content (> 3 wt% TiO_2). Flow features, fractures, graben and small shields and cones associated with RMDSs support their extrusive nature and a genetic relationship with late-stages of host lava flow emplacement and cooling. Some embayment relationships suggest, however, that RMDSs could have formed many hundreds of millions of years to billions of years after emplacement of their host lava units. The documentation of these features has important implications for the understanding of mare basalt eruption and lava-emplacement mechanisms, and for the age and duration of mare basalt volcanism, one of the most important indicators of lunar thermal evolution and mantle geodynamics.

1. Introduction

Morphologic structures and features on and associated with lunar mare surfaces are significant keys to an understanding of the nature of basaltic lava flow emplacement (e.g., Head & Wilson, 2017; Schaber, 1973; Whitford-Stark & Head, 1980; Whitten & Head, 2015; Wilhelms et al., 1987; Zhang et al., 2016), which provides important information on the generation, ascent and eruption of magma and the nature of the lunar mantle (Wilson & Head, 2017b). The recently documented large populations of ring-moat dome structures (RMDSs, Zhang et al., 2017), generally smaller than 1-km-scale, are unique morphologic phenomena in the lunar maria. The earliest description of isolated ring moat structures can be traced back to improved resolution orbital observations of the lunar surface in the 1960s (Schultz et al., 1976; Schultz & Greeley, 1976). Schultz et al. (1976) defined this class of small mare ring moat structures (including ringed dome, ringed cone, and ring moat), characterized by a narrow annular depression, and interpreted these as remnants of flow topography associated with mare emplacement. However, the limited and patchy coverage of high-spatial resolution and low illumination geometry Apollo-era imagery prevented a global survey of these puzzling features.

The ability to characterize the nature and distribution of small geological features such as these has substantially improved in the last decade, due to the acquisition of global high-resolution imagery (e.g., Kato et al., 2010; Robinson et al., 2010), in many cases offering a wide range of viewing geometries and illumination conditions. High resolution altimetry has also been derived from direct measurements (e.g., laser altimetry; Barker et al., 2016 and Smith et al., 2010) or derived from stereo-photogrammetry (e.g., Scholten et al., 2012) and shape from shading (Grumpe et al., 2014; Grumpe & Wöhler, 2014; Grumpe et al., 2018). This allows RMDS morphology to be reconstructed and their volumes to be derived. Zhang et al. (2017) carried out an extensive survey of these bubble-like positive features across the lunar maria and showed that they are characterized by: 1) a generally circular shape and dome-like morphology; 2) a surrounding moat; 3) a relatively small diameter/height ratio compared with other lunar and planetary volcanic features; 4) an occurrence in clusters; 5) an association with the lunar maria, but found only in restricted mare regions; and 6) a composition similar to that of the surrounding lunar maria. Morphologic and compositional analyses of numerous RMDSs supported an extrusive nature and a genetic relationship with the emplacement of local basaltic lava flows (Zhang et al., 2017), although embayment relationships of some RMDSs into depressions interpreted to be impact craters with a variety of degradation states suggests that some RMDS may have formed many hundreds of million years after the emplacement of the flows on which they occur (Basilevsky et al., 2019).

From a large population of more than 8,000 RMDSs identified so far across the lunar maria, including the Moon's nearside and farside (Fig. 1), seven large RMDS-concentration mare regions in the nearside maria are investigated. These basin-interior RMDS-bearing mare surfaces are representatives of the majority of typical mare lava flows on the Moon. The criteria for selecting RMDS areas analyzed here mainly includes two important considerations: (1) these areas chosen have a much larger population of RMDSs compared with other regions in their host basins, and thus a diversity of RMDSs can be comprehensively surveyed; and (2) a series of high-resolution orbital images that satisfy the requirements noted above have been obtained. Therefore, the investigated RMDS regions selected for analysis in this study are focused in Mare Tranquillitatis, Fecunditatis, Humorum, Nubium, and southern Oceanus Procellarum, where a large number of RMDSs are found to be concentrated (Fig. 1).

The main aim of this work is to present data on morphological, compositional characteristic and utilize these data, terrestrial analogs and models of lava flow emplacement to assess the emplacement process of RMDSs, particularly in reference to the underlying mare unit on which they occur. Thus, our analysis provides the opportunity to test the hypothesis of a possible link between lava emplacement mechanisms and flow morphology. The results and conclusions should improve our understanding of the complex interactions (processes that have shaped the lunar RMDSs) between the solid, liquid, and gaseous components of basaltic lava flows on the Moon and to help determine if they are contemporaneous with the emplacement of the lava flows on which they occur or formed much later.

2. Data and Methods

2.1 Data sets used in this study

This study is based on images obtained by the Narrow-Angle Camera (NAC) (Robinson et al., 2010) which is a subsystem of the Lunar Reconnaissance Orbiter Camera (LROC). It provides photometric measurements of the lunar surface at a resolution of down to ~0.5 m per pixel, which is currently the highest available resolution from lunar orbit. There are two parallel monochrome pushbroom cameras, the left NAC and the right NAC, which cover a surface width of about 5 km per track. The available calibrated data contain the so-called "intensity over flux" (IoF) which represents the measured and calibrated intensity divided by the solar flux, i.e., the estimated reflectance of the surface. The NAC images are thus suitable for photometric surface refinement methods, e.g., photoclinometry or shape from shading. The IoF data are accompanied by the selenographic coordinates of the image center and the image corners. Additionally, the position of the Sun is specified in sub-solar longitude, sub-solar latitude and the solar distance. All NAC images are calibrated and remapped to a cylindrical projection of the spherical body which spans a rectangular grid. The first unit vector is the selenographic longitude and the second unit vector is the selenographic latitude. The ground sampling interval is set to 1 m per pixel. All calculations are performed using the USGS ISIS software.

Where necessary, the 10 m/pixel Kaguya TC (Terrain Camera) data (Haruyama et al., 2008a; Kato et al., 2010) are used to facilitate our study. They are available via the website http://darts.isas.jaxa.jp/planet/pdap/selene/. All LROC NAC and Kaguya TC images used here were investigated using the software ArcGIS 10.2. To make the real appearance/shape of high latitude RMDSs display more precisely from NACs, the Lambert Conformal Projection is applied to base maps.

The shape from shading based techniques used here to construct digital topographic models (DTMs) of the RMDSs incorporates lower-resolution stereo or laser altimetry DTM information in addition to the image information. Our DTM construction method is based on the refinement of an existing DTM, the SELENE and LRO Elevation Model (SLDEM) of Barker et al. (2016). The SLDEM was constructed from measurements of the Lunar Orbiter Laser Altimeter (LOLA) and stereo analysis of the SELENE Terrain Camera (Haruyama et al., 2008b, 2012). The SLDEM has been published at a resolution of 512 pixels per degree (~60 m/pixel), covering latitudes between ±60°. The typical vertical accuracy of the SLDEM is about 3-4 m (Barker et al., 2016). The refined DTMs obtained by this method reveal small details comparable in size to the ground spacing interval of the images and are at the same time accurate on large scales due to the incorporation of the lower-resolution DTM information.

Mean elemental abundances and their standard deviations were estimated from Chandrayaan-1 Moon Mineralogy Mapper (M^3) (Pieters et al., 2009) spectral reflectance data (http://pds-imaging.jpl.nasa.gov/volumes/m3.html) of the regions under study, resulting in maps of the abundances of the elements Ca, Al, Fe, Mg and Ti for the RMDS sites.

2.2 Producing NAC-derived DTMs

An extensive survey of the development of reflectance-based methods for DTM production is given by Horn (1990). Additionally, Horn (1990) presents a coupled scheme for simultaneous estimation of surface height and gradients that is referred to as "shape from shading". A similar method was developed by Kirk (1987). Following the reasoning of Horn (1990), Grumpe et al. (2016) introduce the reflectance-based estimates $p \approx \partial z/\partial x$, $q \approx \partial z/\partial y$ of the surface's z gradient field. The introduction of the independent variables p and q, respectively, enables the estimates to deviate from the true gradient field, e.g., due to image noise and model inaccuracies. Horn (1990) introduces the intensity error

$$E_I = \frac{1}{2}\int_x \int_y \left(I - r(\mu_o(p,q), \mu(p,q), \alpha)\right)^2 dx\, dy \qquad (2.1)$$

where the cosines of the incidence angle and the emission angle are denoted by μ_0 and μ, respectively. The squared difference between the measured reflectance I and the reflectance $r(\mu_o(p,q), \mu(p,q), \alpha)$ predicted by the model is integrated over the whole image area. Notably, the incidence angle and the emission angle depend on the estimated surface gradient field.

The intensity error term may be minimized with respect to p and q. However, an unlimited number of gradient field estimates minimizes Eq. (2.1) given that one intensity is measured at each image pixel, whereas two components of the gradient field need to be estimated for each pixel. To place an additional constraint on the gradient field, Grumpe et al. (2014) introduce the gradient error term

$$E_{grad} = \frac{1}{2}\int_x \int_y \left(f_\sigma(p) - f_\sigma\left(\frac{\partial z_{DTM}}{\partial x}\right)\right)^2 + \left(f_\sigma(q) - f_\sigma\left(\frac{\partial z_{DTM}}{\partial y}\right)\right)^2 dx\, dy \qquad (2.2)$$

where z_{DTM} is an existing DTM of lower lateral resolution and $f_\sigma(\cdot)$ is a Gaussian low-pass function of width σ. This additional error term restricts the solution of Eq. (2.1) to be as similar as possible to the gradient field of the existing DTM after a low-pass filter has been applied, i.e., the large-scale trend is inferred from the known DTM.

To recover the surface model z from the estimated gradient field, *Horn* (1990) introduced the integrability error

$$E_{int} = \frac{1}{2}\int_x \int_y \left(p - \frac{\partial z}{\partial x}\right)^2 + \left(q - \frac{\partial z}{\partial y}\right)^2 dx\, dy \qquad (2.3)$$

which aims at estimating the DTM of the surface z which possesses a gradient field that is similar to the reflectance-based estimate. Notably, due to image noise and modeling inaccuracies the gradient field estimate commonly does not possess a potential function and thus a direct integration is not possible.

The absolute depth error

$$E_{depth} = \frac{1}{2}\int_x \int_y \left(f_\sigma(z) - f_\sigma(z_{DTM})\right)^2 dx\, dy \qquad (2.4)$$

is introduced by Grumpe and Wöhler (2014) and further restricts the surface model z to follow the large scale trend of z_{DTM}.

To derive high-resolution DTMs from NAC images, we adapt the reflectance-based DTM refinement method of Grumpe et al. (2016), who combine Eqs. (2.1) through (2.4) into the optimization problem

$$\min_{p,q,z} E_I + \delta E_{grad} + \gamma E_{int} + \tau E_{depth} \qquad (2.5)$$

where δ, γ, and τ are arbitrary weights, respectively. Following Horn (1990), the reflectance-based gradient estimates p and q are supposed to be independent of the DTM z and an alternating iterative update scheme is applied. Consequently, E_{depth} is independent of p and q, and the updated values of p and q can be obtained by minimizing Eq. (2.4) with respect to p and q. The solution is given by Grumpe et al. (2014) and is too lengthy to be repeated here. Furthermore, E_I and E_{grad} are invariant with respect to z and the iterative update rule of Grumpe and Wöhler (2014) is adopted. The algorithm alternates between updating the reflectance-based gradient estimates p and q and updating the DTM z. This update rule is repeated until the convergence criteria of Grumpe and Wöhler (2014) are met or the maximum number of 10,000 iterations is reached. The width of the low-pass filter $f_\sigma(\cdot)$ is set to $\sigma = 15$ pixels. The weights of the error term are set to $\delta = 1 \cdot 10^{-3}$, $\gamma = 1 \cdot 10^{-4}$, and $\tau = 1 \cdot 10^{-2}$, respectively.

The NAC images are of approximately 1 m lateral resolution while the SLDEM is resampled to a grid with approximately 60 m spacing near the equator. To bridge the gap in resolution, a pyramidal approach is applied by downscaling the image by a factor of two until the resolution is less than the resolution of the SLDEM, i.e. the NAC image is downscaled $n_{pyr} = 7$ times by a factor of two which yields an image at a resolution of about 128 m per pixel and the SLDEM is resized to the same dimensions. The downscaled version of the NAC image and the SLDEM are then used to produce a refined DTM at 128 m per pixel resolution. The refined DTM is then upscaled by a factor of two and used as the restricting DTM for another DTM refinement step at a resolution of $n_{pyr} \leftarrow n_{pyr} - 1$. This process is repeated until a refined DTM at 2 m per pixel resolution has been created.

The reflectance-based surface recovery relies on the predicted shading of a reflectance model. Physically motivated reflectance models, which are frequently applied to planetary bodies, asteroids, and comets, are those by Hapke (1981) and Shkuratov et al. (1999). Both model a single particle as a slab and predict its scattering behavior. The surface reflectance is then computed by taking into account multiple scattering between particles in a regolith layer. The main difference between the models of Hapke (1981) and Shkuratov et al. (1999) is the treatment of the single-particle scattering function or "phase function" (Poulet et al., 2002).

Here, we adopt a version of Hapke model which includes anisotropic scattering particles and is given by Hapke (2002)

$$r_{\mathrm{Hapke}}(\mu_0, \mu, \alpha) = \frac{w}{4\pi}\frac{\mu_0}{\mu+\mu_0}\left(f_{SH}(\alpha)p(\alpha) + M(w, \mu_0, \mu)\right)f_{CB}(\alpha)S(\bar{\theta}, \mu_0, \mu) \qquad (2.6)$$

where the cosines of the incidence angle and the emission angle are denoted by μ_0 and μ, respectively. Both angles have been corrected for unresolved surface roughness according to Hapke (1984). The unresolved roughness is modeled by the mean slope angle $\bar{\theta}$. $S(\bar{\theta}, \mu_0, \mu)$ is the correction factor from Hapke (1984). $M(w, \mu_0, \mu)$ represents the multiple scattering inside a layer of regolith which consists of particles whose scattering behavior depends on the phase angle α and is modeled by the phase function $p(\alpha)$. The single-scattering albedo is denoted by w. The shadow-hiding and the coherent backscatter opposition effects are modeled by $f_{SH}(\alpha)$ and $f_{CB}(\alpha)$, respectively.

We apply the method of Grumpe et al. (2015) to compute a locally varying single-scattering albedo w using a Gaussian low-pass filter of width σ_w = 21 pixels. The remaining parameters are adopted from Warell (2004), i.e., the parameters of the double Henyey-Greenstein phase function are set to c_{DHG} = 0.7 and b_{DHG} = 0.21, the terms describing the coherent backscatter opposition effect and the shadow hiding opposition effect are combined and their parameters are set to B_{SH} = 3.1 and h_{SH} = 0.11, and the macroscopic roughness parameter of the Hapke model is set to $\bar{\theta}$ = 11°.

2.3 Measuring diameters, heights, and volumes of RMDSs

The NAC-based high-resolution DTM is used to determine the diameter, height and volume of each RMDS in twelve small mare areas, and each is covered by one pair of LROC NACs (yellow boxes in Figs. 2a and b, and also see Table 1 for details), where the RMDSs are considered to be of a circular outline. The smallest craters visible in our DTMs have diameters around 5 m with depths < 1 m. This shows that our DTMs are sensitive to differences in elevation of < 1 m. These measurements allow for statistical analysis of the interdependencies between these quantities.

Two reference points $\vec{w}$ and $\vec{e}$ on the western and eastern rim for measured RMDSs (Figs. 3a-c), respectively, are marked manually. The RMDS diameter, d, corresponds to the distance between the reference points, i.e., $d = \|\vec{w} - \vec{e}\|$. The average $(\vec{w} + \vec{e})/2$ of the reference points corresponds to the RMDS center.

Then the points $\vec{w}$ and $\vec{e}$ are connected by a line in the DTM raster computed according to the algorithm of Bresenham (1965), and the maximal DTM value $\mathrm{DTM_{max}}$ on the line is extracted. The RMDS height, h, is then computed according to

$$h = \mathrm{DTM_{max}} - \frac{\mathrm{DTM}(\vec{w}) + \mathrm{DTM}(\vec{e})}{2} \qquad (2.7)$$

i.e., the RMDS height corresponds to the difference between the maximal DTM value and the average DTM value of the eastern and the western reference point, respectively (Fig. 3d).

For determining the RMDS volume, the average DTM value on the circular RMDS rim is computed first. It is denoted by $\mathrm{DTM_{rim}}$. The RMDS volume is then obtained by integration over the RMDS area in the DTM. The integral is implemented as a discrete sum over DTM pixels according to

$$V = \sum_{\substack{\text{i,j inside} \\ \text{boundary} \\ \text{of RMDS}}} s_1 s_2 \left(\mathrm{DTM_{ij}} - \mathrm{DTM_{rim}}\right) \qquad (2.8)$$

with s_1 and s_2 as the ground sampling interval of the DTM in east-western direction and north-southern direction, respectively, and $\mathrm{DTM_{ij}}$ as the DTM value at pixel (i, j). The summation is carried out over all DTM pixels located closer to the RMDS center than its radius, $d/2$.

Surface slope information can be estimated based on the elevation dataset. From the NAC-based DTMs, the slope is measured in units of degrees and determined by the rates of change of the surface in the horizontal and vertical directions from two reference points. In this work, slopes were derived using the 'Slope Tool' within the ArcGIS 10.2 platform. Detailed information is available online.

RMDSs and their surrounding mare surfaces commonly exhibit a complex topographic variation (Kreslavsky et al., 2013; Rosenburg et al., 2011). To simplify the technical process of measuring moat depth and width of RMDSs, a moat depth is here defined as the vertical distance between the lowest point of the moat floor and its adjacent RMDS-outward turn point where topography begins to change from rising to level or down (red vertical line, D, Fig. 3d). The horizontal distance between the turning point and its extension to the adjacent RMDS topographic outline is defined as the width of the moat (red horizontal line, W, Fig. 3d). This specific process helps to consistently define moat depth and width in highly variable topography at the local level.

2.4 RMDS density mapping

Of the seven large mare regions, as outlined in Figure 2, R1 in Mare Tranquillitatis has the largest number of RMDSs (about 890, see Table 2) and it is used to perform density mapping to derive statistics about their spatial distribution. The Point Density tool in ArcGIS 10.2 software is used to calculate the density of point features around each reference point, and each point represents the center location of each RMDS. During the calculation, a search radius is defined around each reference point, and the number of points that fall within the circle neighborhood is totaled and divided by its area. Two considerations result in a search radius of 2 km: (1) each RMDS should be counted during calculation considering that all identified RMDSs are between 0.03 to 2 km in diameter; and (2) smaller searching radius values produce a raster that shows more detail, while larger values generate a more generalized result.

2.5 Technique used to perform elemental mapping

To constrain the composition of RMDSs and their surrounding maria, seven expanded large RMDS regions (each region contains several to tens of pairs of NACs, white boxes in Fig. 2) in five nearside basins, including Mare Tranquillitatis, Fecunditatis, Nubium, Humorum, and Procellarum were mapped using full-resolution M^3 data (140 m/pixel, see Pieters et al., 2009) resampled to 300 pixels/degree (~100 m/pixel). These regions were selected because they are areas of highest RMDS concentration in their host mare basins. The twelve small areas, in which RMDSs were quantitatively measured in Section 2.3, are contained within the seven larger regions (Fig. 2). The detailed information concerning each region's host mare, center coordinate, RMDS number, and mean titanium abundance of the RMDSs in each region are listed in Table 2. To construct these maps, previously developed methods for M^3 hyperspectral data analysis (Wöhler et al., 2014, 2017; Bhatt et al., 2015) were utilized. We applied a correction of the M^3 spectral radiances for thermal emission (Wöhler et al., 2017) as well as a correction for topography and normalization to uniform illumination and viewing geometry (Wöhler et al., 2014). For the mare-specific TiO_2 abundance, a resampled nearly global M^3 mosaic corrected in the same way for topography and thermal emission and normalized to the same uniform illumination and viewing geometry has been used. The latitude range of this mosaic is ±75° and its resolution is 20 pixels/degree (~1500 m/pixel). All pixels with a FeO content >13 wt.% were considered as mare areas, which is in accordance with ~30% coverage of mare basalts on the nearside (Head, 1976; Nyquist & Shih, 1992; Qin et al., 2012; Whitten & Head, 2015).

The TiO_2 content was derived from M^3 spectra using the algorithm described by Bhatt et al. (2015). Based on the normalized spectral reflectance data, the TiO_2 content was inferred from the slope of the spectral continuum around 1 μm and the logarithmic ratio of the absorption band depths at 1 μm and 2 μm. Based on the nearly global M^3-derived maps of these two spectral parameters, a second-order multivariate regression function calibrated with respect to the "ground truth" Lunar Prospector Gamma Ray Spectrometer Ti abundance data (Prettyman et al., 2001) was constructed. The FeO, MgO, CaO and Al_2O_3 abundances were obtained by multivariate linear regression based on the continuum slopes around the 1 μm and 2 μm bands, the absorption depths of these bands, and the center position and width of the 1 μm band, where the regression function was again calibrated with respect to the corresponding LP GRS elemental abundances (see Wöhler et al., 2014 for details). The regression functions obtained were used to derive abundance maps of TiO_2, FeO, MgO, CaO and Al_2O_3 for the twelve small mare areas containing RMDSs (Table 3), using full-resolution M^3 data.

Zhang et al. (2017) observed no albedo differences and spectral anomalies of RMDSs relative to their surrounding mare surfaces. However, the mean TiO_2 content of each RMDS in seven large regions (total 2407 RMDSs, Fig. 2 and Table 2) was extracted and compared with the global Ti abundance of all lunar mare regions (latitude range +/-

75 degrees). Each RMDS is considered as a circle with a radius extending to the surrounding moat area. A large portion of RMDSs examined are larger than the M^3 resolution of 140 m (Fig. 4). Due to the absence of compositional differences between the RMDSs and the surrounding surface (Zhang et al., 2017), it can be assumed that the TiO_2 estimates for the small RMDSs are also representative. In addition, for comparison, the other two sets of TiO_2 abundance maps derived from Clementine UVVIS (100 m/pixel, Lucey et al., 2000) and LROC WAC data (400 m/pixel, Sato et al., 2017) were also applied to extract TiO_2 contents of the 2407 RMDS-located sites.

3. Results

Previously it was shown by Zhang et al. (2017) that at least ~2,600 RMDSs are present on the Moon; however, our current survey significantly expanded the number of known RMDSs as we detected more than 8,000 edifices in a large range of nearside and farside mare settings. The newly identified RMDSs (Fig. 1) are mainly distributed in Mare Tranquillitatis, Fecunditatis, and southern Procellarum; for the first time, RMDSs are found in Mare Frigoris (29), and the impact basins Grimaldi (40) and Von Karman (6).

3.1 Statistical characterization of RMDSs

A total of 532 RMDSs in twelve small mare regions (yellow boxes in Fig. 2) were measured and analyzed with regard to their diameters, heights, and volumes (Table 1). Diameters range from 68 to 645 meters (mean and median 209 and 192 meters respectively). The highest RMDS is estimated at 13.4 m, and the lowest ones are < 1 m (mean and median 3.60 and 3.41 meters respectively). The volumes and heights of the RMDSs are shown as a function of their diameters in Figure 4, but the typical volumes of RMDSs with diameters smaller than 300 m are $\leq 1.0\times10^5$ m^3. Lunar RMDSs have average summit slopes of <5° and some steeper margins with up to 10°, in particular for slopes surrounding moat depressions.

We investigated possible significant statistical differences between the Size-Frequency Distribution (SFD) of RMDSs in the three regional settings: Mare Fecunditatis, Tranquillitatis, and Oceanus Procellarum (also see Table 1). The ratio between the maximum height and diameter (h/D) of the RMDSs can be taken as a reasonable classifier due to their typical morphology (i.e., circular positive-relief features). Histograms using a narrow bin size (h/D = 0.01) reveal some unique distribution patterns (Fig. 5a) but within a constrained range ~0.005 to ~0.03, which corresponds to h/D ratios of 1/200 and 6/200. The widest spread of values relates to Mare Tranquillitatis (T, kurtosis -0.14) mostly due to two outliers with outstanding h/D values. Correlations tests indicate a 'strong' affinity between the RMDSs populations in Procellarum and Fecunditatis (P-F, 0.82), 'good' for Fecunditatis and Tranquillitatis (F-T, 0.66), but 'none' between Procellarum and Tranquillitatis (P-T, 0.46).

By enlarging the bin size, thus approaching a line-fitting approach, it is possible to evaluate broad relationships more clearly (Fig. 5b): the most common h/D ratio is 0.02 (or 4/200); Procellarum and Fecunditatis share similar values above this point but differ in the smaller range; and Tranquillitatis' population is skewed towards higher ratios in comparison to the others (i.e., relatively taller RMDSs).

The data plotted in Figure 5c was normalised to 100 to represent the relative weight within each setting expressed as a percentage: for instance, the bin 0.02 (4/200) represents ~34, 37, and 38% of all RMDSs for Procellarum, Tranquillitatis, and Fecunditatis respectively. When viewed in this way, we see that Procellarum and Fecunditatis show comparable overall distribution shapes peaking again at 0.02 but with ratios skewed towards higher h/D values for Tranquillitatis.

The point density map qualitatively suggests non-uniform spatial distributions of RMDSs (Fig. 6); some RMDSs appear to be isolated, but others are concentrated in clusters. The density value (the number of RMDSs/km^2) is estimated to be ≤ 5 per square kilometer with a search radius of 2 km in the central Mare Tranquillitatis region. The regions of highest RMDS density are located on the inclined flanks (elevation/distance = 1:100) of the topographic high (Zhang et al., 2017, and their Fig. 1b). The higher RMDS-density zones (red color, Fig. 6) are characterized by a visual impression of closely spaced convex mounds that occur in clusters or coalesce into dumbbell and chains of varying length (Zhang et al., 2017).

3.2 Elemental abundances in the RMDS regions

We have extracted the mean elemental abundances of Ca, Al, Fe, Mg and Ti for each of the twelve small RMDS areas (yellow boxes in Fig. 2 and Table 3). The twelve RMDS sites are located in basalt regions of moderate to high Ti content between 4.5 and 7 wt% TiO_2 (the highest concentrations found in the lunar maria are about 8 wt% TiO_2, Bhatt et al., 2015). The Tranquillitatis basalts have a particularly high Ti content of up to ~6.4 wt% TiO_2 (Areas 1 to 3, Tables 1 and 2). The other elemental abundances indicate typical mare composition (Bhatt et al., 2019).

The mean Ti content of each RMDS in the seven large regions (white boxes in Fig. 2 and Table 2) was extracted and plotted versus the diameters of RMDSs in Figure 7a. Our M^3 mapping results show that the vast majority of RMDSs have a TiO_2 abundance > 3.5 wt%, while the average TiO_2 content of the RMDSs in each region is between ~5 and 6 wt% (Table 2). Clementine-derived TiO_2 contents of RMDS sites are between ~4 wt% and 16 wt% with >6 wt% for the most RMDS-hosting regions, while LROC WAC-derived TiO_2 contents are between ~3 wt% and 10 wt% with >5 wt% for the vast majority of RMDSs (Fig. 7a). These TiO_2 content values all indicate that the investigated RMDS areas are medium- to high-titanium basalts since low-Ti basalts are commonly estimated to contain < 2 wt% TiO_2 (Sato et al., 2017).

Based on M^3-derived results, the mean Ti contents of RMDSs in seven large regions are compared with the global Ti abundance of all lunar mare regions (latitude range +/- 75 degrees). The histogram of the global Ti abundance (Fig. 7b) for the complete lunar mare surface (latitude range +/- 75 degrees) was derived from a corresponding global Ti map at a scale of 20 pixels per degree and was constructed with the same method as the local Ti abundance maps of the RMDS regions (Bhatt et al., 2015). All pixels with a FeO content >13 wt% were considered as mare areas (Qin et al., 2012).

On average, the RMDSs have a higher Ti content than the maria in total. In comparison with the global mare Ti content histogram, the RMDS histogram is narrower and shifted towards higher Ti values. In Figure 7b, the red and the green histogram denote the distribution of the Ti abundances for the lunar mare areas and the RMDSs, respectively. Both histograms are normalized to 1, such that the sum of all red histogram bins is 1 and the sum of all green histogram bins is also 1. The width of each histogram bin is 0.1 wt%.

3.3 Analysis of topography and morphology

Slopes of the mare regions under study: Lava flows characterized by RMDSs appear to be emplaced on regional slopes less than 2° with low roughness (Rosenburg et al., 2011; Kreslavsky et al., 2013), a range similar to shallower slopes of intermediate and long basaltic lava flows on the Earth (Keszthelyi & Self, 1998). Asymmetric profiles tend to follow the local topography including on the flanks of mare domes (Zhang et al., 2017, and this study), and some RMDSs are found next to terrain depressions (white arrows, Fig. 8a).

Measurements of surrounding moats: Almost all of the population of RMDSs detected are characterized by shallow surrounding moats tens to more than one hundred meters wide and a few meters deep. This is demonstrated by a topographic profile of four RMDSs in area 2 in Mare Tranquillitatis (Fig. 8a). The RMDS-2 in Figure 8a has a broad moat about 200 meters wide, while RMDS-3 shows a narrow moat ~80 meters (Fig. 8b). All four RMDSs display a moat 3 to 5 meters in depth, except for RMDS-3, which has a shallower depth of around ~1 meter. An important observation is that these RMDSs often have a slightly asymmetric topographic profile: the elevation of one of their sides is sometimes a few meters higher than the other side. For example, along the line segment AB (Fig. 8a), the southeastern moat side of RMDS-1 is about 7 meters higher than the opposite side (Fig. 8b), measured from the lowest point of the moat. Of these four measured RMDSs, only RMDS-3 has an approximately symmetric profile but featuring an asymmetric moat.

Depressions in the moat lows and on the mounds: Most lunar RMDSs have gentle slopes, a convex upward profile, and either a complete or incomplete ring moat. A variety of diverse morphologic depressions (circular and/or irregular in shape) is observed associated with numerous RMDSs in many locations, particularly in topographic moat lows or on top of the mounds including both at and off the center (white arrows, Fig. 9).

***Asymmetric topography profiles*:** Most RMDSs commonly show a circular or quasi-circular shape locally extending outward to the surrounding terrain. Morphologic variation from the low-illumination NAC image shows some parts of RMDSs where the moat appears to be filled by mare or RMDS mound material and connected to the surrounding mare surface (white arrows in Fig. 10a). Figure 10b exhibits three RMDSs showing a complex spatial relationship with each other. The largest RMDS is about 550 m in diameter and tangent to a smaller one (~220 m) to its south, which appears as a satellite of the larger RMDS, and this arrangement was previously reported as dumbbell and short chain patterns by Zhang et al. (2017). A small RMDS or lava dome (yellow arrow) is observed on the western flank of the largest RMDS, which partially superposes a ~500-m-diameter impact crater to its northeast.

3.4 Spatial relationship to adjacent mature craters and overall degradation state

Some RMDSs are found adjacent to what appear to be morphologically mature and generally circular depressions (white arrows, Fig. 8a) or even to partially superpose them (Zhang et al., 2017; Basilevsky et al., 2019). In the examples shown here, the mature craters partially superposed by RMDSs (Figs. 11a and 11b) usually exhibit a general symmetric profile of the cavity along the line cutting through superposed RMDSs. An unexpected slope symmetry of the superposed craters is commonly observed (Figs. 11c and 11d). It could be expected that the crater side superposed by the RMDS should have a relatively steeper slope than the opposite side, but this is not observed, as seen in the two examples shown in Figure 11. The two craters are both about 300 m in diameter with a depth of ~15 m (d/D ratio about 0.05). The maximum slope of the walls of the craters is about ~6°, which corresponds to class C impact craters (Basilevsky, 1976) that are considered to have reached 'steady-state' (or "repose angle", i.e., a much reduced gravitational wasting rate) (Basilevsky et al., 2019).

3.5 Flow-like features associated with RMDSs

Flow-like features and/or margins of mare deposits associated with RMDSs are observed, though identifications of distinct lava flow margins are highly uncertain considering that they formed billions of years ago and have been subdued by regolith development. Figures 12a and 12b show two examples of RMDSs and adjacent craters where flow-like margins are evident (white arrows). The two craters are partially superposed by a ~300 and 180 m diameter RMDS, respectively. A flow-like feature located on a side flank of an RMDS (Fig. 12c) extends up to the rim of a degraded crater (white arrow), giving it the appearance of a lava lobe originating from the RMDS. Some pre-existing RMDSs might have been surrounded by subsequent lava flows, which display albedo and surface texture differences from earlier examples (white arrows, Fig. 12d). This increases the morphological complexity of the RMDSs, in particular in relation to the width and depth of the original ring moat.

Preexisting topography is another important factor affecting the formation of lava flow surface features. Short chain patterns of RMDSs are often observed (Fig. 8a, white box), and in some cases they are associated with linear, or sinuous elongate pressure ridge-like flows (Fig. 13). This could be considered as terrestrial analogues of the inflation patterns of compound pāhoehoe flows within which sinuous pathways develop and act as transport systems (Khalaf & Hammed, 2016; Orr et al., 2015; Rader et al., 2017). In some places, one edge of the flow is coincident with the occurrence of RMDSs (white arrows in Figs. 13a and b, RMDS occurrence at the edge of the flow).

3.6 Associations with lineaments, fractures, or graben in RMDS areas

Typically, two prominent types of volcanic structures occur in RMDS-concentration areas: (1) linear fractures or graben, and other dike-emplacement-related lineaments; and (2) shield volcanoes and mare domes. These volcanic features formed during various phases of typical lunar basaltic, dike-fed eruptions (e.g., Head & Wilson, 1993, 2017; Wilson & Head, 2017b, 2018; Klimczak, 2014; Zhang et al., 2016, 2018b).

Three such regions of interest in Mare Tranquillitatis are shown and investigated here. Central Mare Tranquillitatis (Fig. 14a, R1 in Fig. 2a) was first reported by Zhang et al. (2017) to have a very high density of RMDSs. Many RMDSs are situated on the top of a gently-sloping topographic high which is on the average ~100 meters higher than the surrounding lows, across an area of around 25×20 km^2 (Figs. 14b-d). Several NW-SE-orientated lineaments (red and white arrows, Fig. 14a), grooved in places, cut across this region. Of these, four are extensional fractures (red arrows), and the other two are linear positive relief segments (white arrows). An elongated mountain-like feature (yellow arrow) with highly degraded summit depressions is parallel to the two linear fractures and a ridge-like feature to its southeast. To the northeast, we observe two mare domes (white dashed lines), with the larger one featuring a tadpole-shaped summit vent. Some RMDSs occur on its low, flat flanks with a gentle slope of ~0.013 % (<1°). These types of mare domes have a similar morphology to small terrestrial lava shields and are considered to be approximately of the same age as the surrounding lava plains (Head & Gifford, 1980; Head & Wilson, 2017).

The second instance is an area of high RMDS concentration contained in region 2 of southwestern Mare Tranquillitatis (R2, Fig. 2a). This area includes three major linear fractures oriented in a NW-SE-trending direction (white arrows, Fig. 15). The bottom one is a prominent graben, over 700 meters wide in places with a length of over 18 km. It appears to consist of two linear rille-like segments connected by elongated depressions, suggestive of graben-like subsidence. The linear feature is also punctuated by intact, roofed sections or walls that have not collapsed between elongated pits. From the high-resolution NAC images, copious rocks and fragments of different sizes can be observed to have accumulated on the rille walls. To its north and northeast, we see two other graben about 400 m wide with relatively shallow, flat floors which are bounded by two steep-sided walls that run parallel to each other. These NW-SE-trending extensional structures exhibit a pattern radial to the Imbrium basin, suggesting a possible association with the effects of the Imbrium impact structure.

The northern Mare Tranquillitatis region neighboring the Gardner shield volcano complex (Spudis et al., 2013; Tye & Head, 2013; Wood et al., 2005; Zhang et al., 2018b) contains scattered km-scale volcanic shields and mare domes with or without elongated summit vents or fissures (white dashed lines, Fig. 16). They are interpreted as localized volcanic extrusive materials similar to terrestrial shield volcanoes (Tye & Head, 2013; Wilhelms, 1972). Some are arranged in a line radial to the Gardner shield and Mare Serenitatis and thought to have been controlled by impact-induced faults/dikes (Lena et al., 2013; Wöhler et al., 2007; Zhang et al., 2018b). Two volcanic lineaments (red dashed lines, Fig. 16), named as "cones of Mons Esam" by Weitz and Head (1999), show an *en echelon* pattern consistent with the surface expression of a dike (Ernst et al., 1995) and may have formed by degassing of a near-surface dike (Head & Wilson, 1993; 2017). The three regions with superposed elongated NW-SE-trending depressions (white arrows, Fig. 16) were also mapped as mare domes by Wilhelms (1972). These elongated summit vents provide evidence of the orientation of the dike through which magma ascended to the surface (Head & Wilson, 2017). These very low aligned domes in northern Mare Tranquillitatis were interpreted to have formed from low-Si/high-FeO basaltic lavas with moderate titanium content (Lena et al., 2013). A series of RMDSs are located on and/or around these shield volcanoes and mare domes.

3.7 Relationships between the distribution of RMDSs and Irregular Mare Patches

Some flow regions surrounding Irregular Mare Patches (IMPs, Braden et al. 2014) are populated with RMDSs, while at many RMDS locations, IMPs are not found. For example, a RMDS-like mound stands ~2.5 m higher than the surrounding floor surface of an IMP located in western Mare Tranquillitatis (Figs. 17a and b). About 1 km away, to the northwest of the IMP, there is a ~500-m-diameter RMDS with a moat ≥ 100 m in width

(Fig. 17c). Based on the NAC-derived DEM, the moat has an average depth of about 2 to 3 meters, which contrasts with the IMP depression of less than 1 m depth around the mound (Fig. 17d). The ring depressions around RMDSs have a depth range similar to that of the topographic moats (several meters) adjacent to the irregular mounds across the Ina depression (Garry et al., 2012; Qiao et al., 2019), but a width commonly larger (tens to hundreds of meters) than that of IMP mounds (several to tens of meters).

Close associated IMP and RMDS features are also observed to occur at the boundary of a volcanic vent. The volcanic vent is situated at the summit of a volcanic edifice, which is characterized by a nearly north-west-trending pit crater cluster on its top (Fig. 18a) with the detailed morphologic information shown in the topographic map (Fig. 18b). This volcanic vent includes two step-like platforms (Fig. 18c) suggesting discrete eruptive episodes. The IMP-RMDS association occurs at the southwest boundary of the lower platform (white dashed box, Fig. 18c) and perhaps indicates their formation during late-stage eruptions. A series of IMPs and RMDS-like units can be seen from the high-resolution 1.22 m/pixel NAC image (Fig. 18d). These RMDSs are smaller in diameter (in the order of tens of meters) in comparison with the average of 100-400 m (Figs. 4 and 7a). The occurrence of the pit crater cluster follows the trend of a possible subsurface fracture indicating dike-fed style eruptions (Zhang et al., 2018b; their figure 12). The geologic background of this area, which overlies a positive quasi-circular gravity anomaly with low topography (Zhang et al., 2018b; their figure 10), supports such eruptions through the channels controlled by subsurface tectonic structures.

4. Discussion

Based on the investigation of ring moat structure clusters in the Flamsteed Ring, in southern Oceanus Procellarum, Schultz et al. (1976) hypothesized four different formation mechanisms for ring-moat structures: (1) pseudo-vents, (2) volcanic vents (such as small tephra cones), (3) pre-flow relief surrounded by later lava flows, and (4) tumuli. The first two scenarios are not likely due to the absence of vent features with only a very small subset displaying summit depressions/craters: their origin as impact craters, collapse pits, or vent features cannot be determined from imagery (Zhang et al., 2017). Additionally, the number, spatial density and clustering of RMDSs are not easily compatible with magmatic eruptions fed by numerous separate volcanic conduits rooted deeper in the crust/mantle. The third hypothesis cannot explain the circularity of RMDSs and their similar composition and morphologic connection to the surrounding maria. The 'tumuli' hypothesis (4) also seems unlikely when we compare RMDSs with terrestrial tumuli, which are controlled by subsurface topography (e.g., a lava tube system), and typically exhibit elliptical or irregular shapes. Also, nearly all tumuli feature a fracture system on their summit with a major crack along the strike. However, crack or fracture features are not observed on any of the RMDSs observed so far, but this may be due to subsequent degradation and filling by regolith formation. Importantly, no observable ring depressions have been reported around tumuli on either Earth or Mars (e.g., Diniega et al., 2018; Duraiswami et al., 2001; Rossi & Gudmundsson, 1996; Self et al., 1998; Walker, 1991).

The RMDSs are distributed over a broad area, rather than narrower zones that might represent a rift/fracture volcanic system. It seems reasonable, therefore, to suggest that a plausible RMDS formation mechanism might involve some kind of endogenic process occurring at the time of emplacement of the RMDS-host lava flows. This is consistent with the previous general idea of a remnant of flow topography associated with mare emplacement (Schultz et al., 1976). Although a global survey of RMDSs continues, we consider that RMDSs are an important geological feature characterizing the lunar maria.

4.1 Morphological Associations between RMDSs and Surroundings

Due to the low mound height and shallow moat depressions, a comprehensive global survey of RMDSs requires full global coverage of high spatial resolution images with low sun illumination conditions, i.e., a solar incidence of ≥60°, to produce elongated shadows and highlight subtle morphology variations. The availability of such products has yet to reach global coverage, and thus the global distribution mapping of such small-scale (tens to hundreds of meters) lunar RMDSs is a long-term project requiring detailed analysis of not yet available data (see discussion in Section 5). However, the RMDS subsets analyzed were selected from a large population of more than 8,000 RMDSs identified so far, and the selection was designed to represent typical RMDS cases with sizes ranging from tens to hundreds of meters occurring in a large range of mare settings.

Lunar ring moat dome structures are closely associated with the host basaltic lava flows in which they are located. Sections of their moats appear to be infilled by mare or

RMDS mound material and connected to the surrounding mare surface (Fig. 10a). The asymmetric topography profiles of the ring moat (Zhang et al., 2017) might be controlled by preexisting topographic irregularities. The long axis of some oval-shaped RMDSs may be indicative of a direction or trend that the lava flow or the RMDS formation has followed (Fig. 10a, white arrows point to the contact places connecting the RMDS edifice to the surrounding mare). This is also supported by our compositional mapping results showing no evident variations between RMDSs and adjacent maria, further verifying the initial result that RMDSs showed no spectral anomalies in the region (Zhang et al., 2017). Direct evidence for their genetic relationship with localized host lava flows is suggested by some NAC observations of some apparent flow-front traces in association with RMDSs and the flow-like morphologies nearby (Fig. 12).

Very importantly, there is significant evidence that contradicts a RMDS formation mechanism that is directly related to the emplacement and cooling of the host lava flow unit. Some RMDSs are found adjacent to terrain depressions (mature craters) or even partially superpose them (Fig. 11) (Basilevsky et al., 2019; Zhang et al., 2017) and lead to the conclusion that the RMDSs formed hundreds of millions of years to several billion years following the emplacement of the host lava flow unit. Two hypotheses with regard to the origin of these depressions have been analyzed as follows: (1) the depressions are of impact crater origin and predate RMDSs; and (2) they might have formed by non-impact processes.

Impact craters predating mounds: In this case, such RMDSs cannot form at the same time as the host basalt unit because the time interval between impact craters of this size to be superposed on a flow is very likely to be much longer than the solidification time of a lava flow and any related RMDS activity. Furthermore, the age of emplacement of such RMDSs can be determined by the degradation age of the crater they superpose (Basilevsky et al., 2019). The fact that the depressions overlapped by RMDSs look like "normal" degraded impact craters (Fig.11) raises some concerns about the embayment relationships as one would expect the embayment to produce measurable asymmetry in the crater interior profile. In addition, impact craters completely predating flows would have been embayed or flooded, but larger pre-existing impact craters may indeed cause flexure of the flow upper thermal boundary layer as it is emplaced, resulting in a depression on the top of the flow. If the time span between lava flow emplacement and RMDS formation is short, this would predict only a small number of craters overlapped by RMDSs, consistent with our observations. Fundamentally, however, as demonstrated by Basilevsky et al. (2019), there are multiple examples where both the stratigraphic relationships and the apparently embayed crater degradation ages strongly suggest that the mound embayed the crater-like depression much later, possibly in the order of hundreds of millions years. Thus, many, if not all RMDSs could have been emplaced over the subjacent lava flows, well after they had completely cooled and solidified.

Collapse pits or lava-rise (inflation) pits in the lava flows: It is possible that some of these craters superposed by RMDSs might form endogenically, by the collapse of more vesicle-rich or volatile-rich parts of the lava flow (e.g., Qiao et al., 2020). Alternatively, some of them could be lava-rise (inflation) pits which form where lava inflation does not occur due to pre-flow topographic control (e.g., Elshaafi & Gudmundsson, 2019; Garry et al., 2012; Walker, 1991). Such pit craters generally should be rimless.

We address these competing assessments of the age of emplacement of RMDSs (1. Related to emplacement and cooling of host lava flows, and 2. Postdating emplacement of host lava flows by up to several billion years) in subsequent sections and the synthesis (Section 5). We now turn to an assessment of the general characteristics of lunar lava flows, terrestrial analogs, and related models for RMDS formation and evolution.

4.2 Lunar Basaltic Lava Flow Evolution

What processes might favor the formation of RMDSs in the context of the emplacement of a lava flow with which they are closely associated? On the Moon, eruptions began when molten or partially molten mantle rocks are transported from the deep mantle to the surface, forced by buoyancy caused by the density difference between the melt and surrounding rocks, and accompanied by the generation of pressure due to exsolution of volatiles. Typical eruption rates are predicted to lie in the range from 10^4 to 10^6 m^3s^{-1}, modelled from magma sources at great depth (Wilson & Head, 2017b). Resulting lava flows can be wide-ranging in morphology and morphometry but a typical example might commonly be ~200 km in length, 10-20 km wide and often >10 m thick. When the lava flow advances, the surface heat flux governs the cooling rate of a thin surface layer (Head & Wilson, 2017).

The very low-viscosity and highly fluid properties of lunar basaltic lava favor initial emplacement as thin, rather than thick sheets of lava, like the tholeiitic Hawaiian basaltic lava (Hon et al., 1994). The absence of an atmosphere on the Moon slightly reduces the cooling rates of flow tops and margins (Head & Wilson, 2017). Convective heat loss is absent, and conduction to the substrate below the flow and radiation from the upper surface dominates heat loss. These lava flow cooling processes result in increasingly thick upper, marginal and lower thermal boundary layers with increasing distance from the vent over time. In addition to the styles and rates of eruptions that fundamentally control lava flow morphology (e.g., Wilson & Head, 2018), the thickness and behavior of the solidifying crust (bending, disrupting, or cracking) exerts important control over the final flow appearance (e.g., Gregg, 2017; Head & Wilson, 2017; Hon et al., 1994; Rader et al., 2017; Self et al., 1998; Wilson et al., 2019).

Once a coherent, insulating solid crust of an active lava flow is formed, it will protect the interior from rapid heat loss and allow new lava to be injected beneath and the subsequent inflation process will lift it upwards as the pressure builds from the molten interior (e.g., Bernardi et al., 2015; Chitwood, 1994; Hon et al., 1994; Self et al., 1996; Walker, 1991). Our compositional mapping results show that RMDSs preferentially form in more Ti-rich magmas, which have lower values of viscosity compared with low-Ti basalts (Williams et al., 2000). This is consistent with terrestrial observations that the inflation process tends to occur in low-viscosity basaltic eruptions (e.g., Rader et al., 2017; Bernardi et al., 2019). The lower gravity on the Moon and the absence of an atmosphere result in a propensity of lava flows to retard lateral spreading and produce less resistance to upward inflation, causing considerably greater thicknesses and widths of lunar lava flows than is common on Earth (Keszthelyi et al., 2000; Keszthelyi & Self, 1998). Horizontal vesicle sheets at the base of the vesicular upper crust arranged in horizontal zones (Cashman & Kauahikaua, 1997; Keszthelyi & Self, 1998; Self et al., 1997; Thordarson &Self, 1998), an indicator of inflated pāhoehoe lava flows (Self et al., 1998), have been observed and sampled in the walls and flanks of Hadley Rille by the Apollo 15 astronauts (Keszthelyi, 2008). The inflation-like endogenous growth of the lava flow (injection of large amounts of lava into the flow, accompanied by gas phases; as is typical for pāhoehoe sheet lobe emplacement (Hartley & Thordarson, 2009; Thordarson & Self, 1998)) thus is also predicted to occur under lunar conditions (lower gravity and nearly vacuum surface environment), and result in a much lower cooling rate of lava flows, but its emplacement may differ significantly from on Earth, producing a set of different flow shapes, structures, and surface features (Head & Wilson, 2017; Wilson

& Head, 2017b, 2018; Wilson et al., 2019).

4.3 Comparison with Inflated Lava Flow Features (Tumuli) on Earth

Lunar RMDSs share some similar attributes with terrestrial lava inflation structures known as tumuli, commonly found in most pāhoehoe lava flow fields (the primary mode of terrestrial flood basalts (e.g., Hon et al., 1994; Self et al., 1996)), such as Hawaii, USA (Hon et al., 1994; Swanson, 1973; Walker, 1991), Etna, Italy (Calvari et al., 2003; Guest et al., 1984), Iceland (Mattsson & Höskuldsson, 2005; Rossi & Gudmundsson, 1996), and Deccan, India (Duraiswami et al., 2001, 2002); they also differ in some key aspects. Tumuli are dome-shaped crustal uplifts resulting from lava inflation processes due to a pressure increase within the hot liquid lava core beneath the already-chilled rigid crust (Walker, 1991) or later inflation localized in preexisting surface depressions (Duraiswami et al., 2001; Rossi & Gudmundsson, 1996; Self et al., 1998) or areas where an interior lava-conveying channel (lava tube) clogged (e.g., Duraiswami et al., 2002, 2004; Guest et al., 1984), allowing a localized buildup of hydrostatic pressure within the fluid core. The low-slope tumuli are comparable in scale to the relatively smaller lunar RMDSs (<100 m), are roughly circular to elliptical in map view, have shallower flanks, and do not display extensive outflows from the cracks (Rossi & Gudmundsson, 1996). The heights of terrestrial tumuli typically correspond to 1−5 m, and in some cases exceed 10 m (Anderson et al., 2012; Chitwood, 1994; Khalaf &Hammed, 2016; Németh et al., 2008; Stephenson et al., 1998; Walker, 1991; Wentworth & Macdonald, 1953), a range similar to RMDSs, which have an average height of ~3.5 m, and the tallest one exceeds 13 m (see Section 3.1). Topographic moats, with depths of a few meters, usually occur where lava embays a mound or inflated sheet lobe (Garry et al., 2012). However, no RMDS-like ring moat is observed for terrestrial tumuli.

The spatial arrangement patterns of RMDSs are reminiscent of a certain kind of distribution pattern of tumuli in terrestrial lava flow fields. Many discrete tumuli are observed on “hummocky” flows produced by lava emplaced slowly and discontinuously on a rough, inclined surface (Self et al., 1998). Tumuli characterized by low slopes tend to have larger sizes and occur in clusters (Walker, 1991). Likewise, this type of spatial organization is seen in RMDS concentration regions (Zhang et al., 2017). In some cases, RMDSs occur in a linear trend (chains or elongation in shape, Figs. 8a, 10b, and 13), consistent with terrestrial analogues of tumuli that appear to be aligned, owing to the geometry of the flow being limited to a narrow width (Duraiswami et al., 2001; Walker, 1991). A clear link between tumuli and the nature of the subcrustal flow pathways has been observed (Anderson et al., 2012 and references therein). If the lava is confined by the topography, such that the lava is prevented from flowing freely, several aligned tumuli or a single elongated tumulus can be formed (Duncan et al., 2004; Glaze et al., 2005; Kauahikaua et al., 1998; Keszthelyi & Pieri, 1993; Orr et al., 2015; Self et al., 1998). Likewise, we also observed that some RMDSs are associated with locally sinuous flows or possible pressure ridges (inflation of narrow tube-fed basaltic lava flows) in mare lava flow fields (Fig. 13). This can be best explained by the flow advance being restricted into narrow pathways by existing topography, such as a surface lava channel. It is possible to envisage a surface channel confining a lava flow into a single continuous feature, sometimes with a pronounced sinuosity. In some places one edge of the flow is coincident with the occurrence of RMDSs, a pattern similar to that some tumuli are found to be located near tubes (Duraiswami et al., 2004; Greeley & Hyde, 1972; Guest et al., 1984). The lateral expansion of the lava flow may be prevented by such structures.

RMDSs, however, were rarely observed occurring in association with such well-displayed sinuous flows or pressure ridges as our survey work was extended to more areas. We cannot rule out a tectonic compressional ridge as a possible explanation for this feature. The formation of elongate, ridge-like tumuli or tumuli alignment over a well-established lava tube has been documented by many authors (e.g., Bernardi et al., 2015; Cashman & Kauahikaua, 1997; Chitwood, 1994; Duncan et al., 2004; Glaze et al., 2005; Kauahikaua et al., 1998; Keszthelyi & Pieri, 1993; Khalaf & Hammed, 2016; Pasquarè et al., 2008; Orr et al., 2015).

Earth flow-lobe tumuli sometimes occur in the middle and lower flanks of shield volcanoes (Rossi & Gudmundsson, 1996), which is probably a close analogue to the occurrence of variable-sized RMDSs on low mare domes, as shown in Figures 14 and 16. Based on this evidence, we propose that late-stage basaltic lava flows with a viscosity between 10^2 to 10^4 Pa s, possibly up to 10^6 Pa s (Lena et al., 2013; Wöhler et al., 2007), could have contributed to the formation of some RMDSs.

There is evidence for a time range for the formation RMDSs relating to their geological setting. Mare domes have been interpreted to represent the last products of regional volcanism, characterized by a lower effusion rate and relatively low temperature of eruption (Lena et al., 2013). These very low mare domes in northern Tranquillitatis exhibit very gentle rises of mare topography and their margins tend to merge gently with surrounding terrain (Fig. 16). According to the dome classification scheme defined by Head and Gifford (1980), these mare domes with lower topographic relief belong to their class 3, a class that is distributed in many mare regions. RMDSs occur in association with domes that are thought to have originated at different times, from a range of depths, and with different compositions (Lena et al., 2013). These observations suggest that RMDS generation does not need to be restricted to a specific time among eruptive sequences, but might be the product of normal mare basaltic lava flows controlled mainly by flow emplacement processes and the preexisting topography (such as low gradient terrains) (Head & Wilson, 2017; Wilson & Head, 2018).

A key difference between terrestrial tumuli and lunar RMDSs is that tumuli often have deep axial cracks (lava inflation clefts, up to 8 m in depth) occupied by squeeze-ups in and on their tops (along with the flow direction) and breakouts from their flanks (Duncan et al., 2004; Glaze et al., 2005; Hon et al., 1994; Keszthelyi & Pieri, 1993; Khalaf & Hammed, 2016; Orr et al., 2015; Rossi & Gudmundsson, 1996; Self et al., 1998; Walker, 1991), which are not observed in lunar RMDSs. Nonetheless, a lava lobe at the foot of a RMDS (Fig. 12c) and a small dome-shaped extrusive feature at the western flank of a RMDS (Fig. 10b, yellow arrow) are observed, supporting the extrusive nature of their formation. This is similar to the cases in which large tumuli sometimes serve as the source for breakout flows and/or additional nearby tumuli (satellite tumuli; Duncan et al., 2004). However, terrestrial tumuli are smaller (most <50 m in length with a few slightly larger than 100 m; Anderson et al., 2012) by a factor of about 10 to 100 than typical lunar RMDSs (tens of meters to slightly larger than 1 km). Inflation-related morphologic, structural, and textural features have also been identified in the martian context (e.g., Diniega et al., 2018; Giacomini et al., 2009; Keszthelyi et al., 2008), but these studies document very similar shapes and sizes (~10 m in width; Diniega et al., 2018) for tumuli on both Earth and Mars, with distinct axial and radial fractures on their tops. The surface textures, lineations and broad folds related to terrestrial inflated sheet flows (Garry et al., 2012) are also absent in the lunar RMDS regions but may be modified or destroyed by later regolith formation.

Inflationary and depletory processes could combine to produce the morphological features of the RMDSs. Subsequent draining, differential deflation, and cooling of the inflated surface could account for the formation of non-impact depressions/collapses within the moat and on the mounds, as illustrated in Figure 9. An alternative explanation for the absence of tumulus-like fractures/cracks might be that they were indeed present but the cracks gradually eroded through regolith-forming effects and seismic shaking (from both impacts and moonquakes). For a single lava flow on the lunar surface, the thickness of regolith on its surface develops at a rate of ~5 to 10 mm Ma^{-1} (Fa et al., 2015; Hörz et al., 1991), and that means a ~5 to 10 m thickness of regolith will be built up within the next 1 Ga after the emplacement of the flow. The median regolith thickness was estimated to be in the range between 2.5 m to 8.7 m from LROC images (Bart et al., 2011), while an average mare regolith layer thickness of ~5 m was obtained from radar and optical data analysis (Shkuratov & Bondarenko, 2001). Based on an average height of ~3.5 m for these 532 RMDSs, some might be wholly made up of regolith.

The behavior of boulder tracks on the lunar regolith indicates that the filling rate of shallow depressions is 5 ± 3 cm Ma^{-1} (Arvidson et al., 1975). Accordingly, 1 m deep cracks in a 1 m thick regolith layer are filled within ~12.5-50 Ma. This could explain why the RMDSs lack fractures or cracks since they appear to be old surface features with the same (or similar) age as the surrounding mare surface (Zhang et al., 2017). Alternatively, the regolith movement or slope mass-wasting could also exert significant influence on the crater size and appearance, causing, for instance, the disappearance of small craters on their surfaces, thus resulting in very young age estimations based on the crater counting method (Zhang et al., 2017). The development of regolith on the surface of several billion year lava flows and RMDSs associated with the time of emplacement also raises the question of how the morphology and morphometry of such ancient RMDS features could survive the development of such a relatively thick regolith, or whether their distinctiveness is evidence for an age younger than the mare substrate on which they form (e.g., Basilevsky et al., 2019).

4.4 Magmatic Foam-Mound Hypothesis

The characterization of lineaments, fractures, or graben in RMDS-rich areas can help in the understanding of the local geologic setting and the eruptive environment associated with their formation. These negative or positive lineaments, as illustrated in RMDS-rich areas (Figs. 14-16), are probably indicative of surface expression of subsurface dikes (e.g., Ernst et al., 1995; Head & Wilson, 2017). The RMDS-rich mare lava flows surrounding these linear surface dike manifestations could thus have been the products of late stage dike-related eruptions. Additionally, a medium to high TiO_2 content range, as estimated for a large population of RMDSs (see Section 3.2), is usually associated with younger mare (Sato et al., 2017), indicating that these RMDSs-hosting mare basalts may be products from partial melting of late-stage cumulates.

Commonly, lunar eruptions are likely to be fed by dikes delivering deep mantle melts (mafic to ultramafic magmas) to the surface (Wilson & Head, 2017b). A significant fraction of the lunar interior may have a water content similar to the Earth's upper mantle, which is estimated from laboratory analysis of lunar pyroclastic beads and melt inclusions (Hauri et al., 2011; Saal et al., 2008). Basaltic partial melting source regions have a depth of below 200 km or more (Elkins-Tanton et al., 2011; Grove & Krawczynski, 2009; Hess, 2000). The presence of water helps facilitate partial melting by reducing melting temperatures. In addition, water makes failure relatively easy to occur by reducing strength (Frohlich & Nakamura, 2009), which is favored by the correlation between mare basalts and deep moonquakes (Qin et al., 2012).

Lunar eruptions develop through three major eruption phases: a steady, high volume flux hawaiian-style explosive stage; an intermittent, lower volume flux strombolian explosive phase; and a final very low volume flux effusive stage (Wilson & Head, 2017a, 2018). A significant difference between lunar and terrestrial mafic eruptions is the occurrence of magmatic water exsolved in the waning stages of eruptions. Water vapor release in lunar magmas at near-surface <500 m depth during the waning stages of dike emplacement events can produce a unique formation, described as "vesicular foam" by Wilson and Head (2017a, 2018). The injection of later lava containing dissolved water into the already-emplaced, nearly stagnant flows will produce very vesicular foam layers within the flow, due to crystallization and gas release, as the lava cools as a function of time. The vesicularity of the foam is subject to the overlying pressure. The pressure at a given depth below the surface of a basaltic lava flow on the Moon is much smaller than on Earth. This is due to the absence of atmospheric pressure and the lower gravity. As a result, on the Moon larger volumes of gases will be exsolved during the second boiling phase than on Earth (Wilson et al. 2019) due to the pressure-dependence of volatile solubility causing a greater growth of gas bubbles. Thus, we would expect flows to be systematically thicker and more vesicular on the Moon than on Earth. Therefore, the final stage lava extruded from dike emplacement could be characterized by the types of lava crusts and foam extrusions interpreted to have formed in the Ina pit crater floor (e.g., foam mounds underlain by a layer of macrovesicular crust; Qiao et al., 2017, 2019; Wilson & Head, 2017a).

RMDSs are bulbous bumps standing above the lava flow surface, in a manner similar to terrestrial analogs with inflated lava flows (See Section 4.3 for detail). With emplacement and gradual cooling of basaltic lava flows, an increase in vapor pressure, due to late-stage injection of volatile-rich hot lava and crystallization of the melt, could crack the overlying quenched crust causing gas emissions and extrusions of magma-volatile mixed materials. This inflation process is enhanced in the low-gravity and low-sloped basaltic environments on the Moon (Wilson & Head, 2018), compared to the Earth (Keszthelyi & Self, 1998).

Based on the final effusive products predicted from the modelling of the process of terminal dike closure and extrusion of magmatic foam (Wilson & Head, 2017a), the erupted lava flow in the vent and the near-vent area will likely form a rough-surfaced layer, characterized by a mixture of Strombolian ejecta and (very) vesicular lava. Any eruptive structures associated with the overlying magmatic foam will be created around and downslope from the vent. An example would be the rough-surfaced Strombolian ejecta surrounded by magmatic foam structures, giving rise to IMPs (Wilson & Head, 2017a). Our discovery of an IMP-RMDS-association at the rim of a volcanic vent (Fig. 18) also suggests that RMDSs and IMPs can form concurrently in the same lava flow field under certain conditions, although the precise mechanism is unclear at present. However, this suggests that both of the features (RMDSs and IMPs) are extrusive in nature (accompanied by endogenous processes such as degassing) and have a genetic relationship with localized lava flows. The geometric measurement of typical dikes on the Moon suggests an average 5 m thick foam layer covering an area of the order of 5−10 km^2 (Wilson & Head, 2017a).

Inflation processes play a key role in the late-stage emplacement dynamics of lava flows on both Earth and other terrestrial planets and their satellites (Kolzenburg et al., 2018). The behavior inferred for many long lava fields on Earth (Aubele et al., 1988; Hon et al., 1994; Self et al., 1996, 1997, 1998; Thordarson & Self, 1998) reveals that the injection of later magmatic volatile-rich liquid into the almost stationary flows may be the key requirement for the formation of RMDSs (Wilson & Head, 2018; Zhang et al., 2017). The eruption and injection of magmatic foam (Mangan & Cashman, 1996) into a crusted lava flow core (insulated by an overlying cooling crust) will undergo gas exsolution and concentration processes due to crystallization and vesiculation in the melt at second boiling phase (Self et al., 1997; Wilson et al., 2019). Once molten lava becomes stagnant or trapped due to topography or flow front solidification, the remaining gas bubbles should rise to accumulate at the base of the upper crust exerting an upwards pressure. Additionally, the cooling of silicate rocks can also result in tensile stress exceeding their tensile strength (Savage, 1978). The concurrence of the gradually increasing pressure and excess tensile stresses could have acted on the cooling upper part of the lava flow by initiating upwelling and fracturing within the upper crust so that the underlying magmatic foam (perhaps driven by a Rayleigh-Taylor instability, Wilson et al., 2019) could have extruded out onto the surface to form mounds. The very vesicular nature of the lava observed in the center of tumuli due to pressure release (e.g., Ollier, 1964) provides a good analogue for the case of RMDSs on the Moon.

Inflationary processes often produce crustal fractures through which extrusions can occur. Compared to the Earth, the lower lunar gravity and the absence of an atmospheric pressure allows for greater inflation, resulting in the generation of more volatile-rich lava extruded onto the surface. This could explain why RMDSs are on average larger than terrestrial tumuli by a factor of 10 or more in magnitude (average ~200 m vs. <20 m in diameter). The original crustal fractures are filled in by lava originating from beneath the lava flow crust and overlain by an extrusive mound, a scenario that is consistent with the lack of visible fractures on RMDSs so far observed. Other fracture features on RMDSs and surrounding mare formed during the cooling process would have been eroded through regolith-forming processes. Ground shaking caused by exogenous and endogenous processes, e.g., impacts and moonquakes (also see section 4.3 for more information) would have redistributed loose material that would end up filling the voids over geologic time.

Regular meter-sized rock boulders are observed on the rims of a few impact craters, which are superposed on RMDSs and appear to be of a young age of the order of several tens of Ma based on their morphologic characteristics (Basilevsky et al., 2019). It seems likely that these impacts might have occurred in a massive rock target, not in thick magmatic foam. However, two possible-scenarios should be considered for the generation of meter-sized boulders by impact cratering processes. On one hand, when a RMDS formed, blocks or fragmented lava crust will be generated by collapse due to removal of the underlying lava (as is always the case for tumuli, e.g., Walker, 1991; Rossi

& Gudmundsson, 1996). These blocks and fragments are overlain by extruded lava mound material; thus, they could have survived billions of years of space weathering effects (i.e., regolith formation, McKay et al., 1991). The upper layer of the RMDS mounds might also have contained fine regolith produced by the mechanical pulverization of fractured, broken crust formed during the RMDS formation-related inflation process. This allows the possibility that impacts on RMDSs might have penetrated the more densely populated substrate to excavate underlying meter-sized rock boulders observed on the rim and inside some young superposed craters (Basilevsky et al., 2019).

Alternatively, large coherent blocks of variable-size welded particles could have formed during impacts on relatively loose materials, producing lunar regolith breccia (A good workbook describing regolith breccias is available via the website: https://www.lpi.usra.edu/lunar/samples/RegolithBrecciaWorkbook.pdf). Extensive studies of lunar meteoritic samples (e.g., Joy et al., 2010) suggest that lunar regolith breccia samples mostly originate from (very) shallow stratigraphic horizons, between 2 m to less than 100 m (Warren 1994). Therefore, blocks could have formed entirely on loose surfaces. In addition, the solidified magmatic foam material may be intrinsically strong enough and be the source of the coherent materials. The key difference relates to the geometry of craters formed in massive rocks and regolith (typically bowl-shaped when fresh) versus craters formed in the magmatic foam: the latter should have smaller diameter to depth values. If the RMDS surface layers were relatively thin (average 3-4 meters in this study, commonly < 5 m of minimum value for normal regolith thickness; e.g., Fa et al., 2015), the impact would have penetrated into the underlying material producing a bowl-shaped crater with a terrace at the boundary of RMDS material and underlying material, forming a so-called concentric crater (e.g., Oberbeck & Quaide, 1967). However, this type of terrace feature is not observed because they have undergone a long period of morphological degradation beginning from their formation. Further, very high-resolution DTMs needed to observe such subdued features are currently not available. Therefore, interpretation of the morphology of the apparently bowl-shaped crater described by Basilevsky et al. (2019) as evidence against the magmatic foam-mound hypothesis remains uncertain.

The extrusion of foamy lava must produce subsurface voids of varying size in the interior of basaltic lava flows, thus exerting a certain influence on the final appearance of the mounds and their surrounding terrains. Topographic depressions associated with RMDSs (Fig. 9) may be caused by a deflation mechanism linked either to outgassing or magma/lava drainage. In some instances, the depression might also be linked to a post-RMDS formation impact event, although the feature is unusually shaped and devoid of diagnostic ejecta features.

According to the dynamic analysis of foam mound formation in late-stage lunar lava lakes, Wilson and Head (2017a) concluded that with an erupted volume flux of 0.6 m^3s^{-1} a typical effusive foam mound should take about nine Earth days to form and eventually have a volume of ~4.6×10^5 m^3, an estimate within the top range of our measured volume for 532 RMDSs (Fig. 4b). The estimation of the measured volumes of the 85 identified mounds on the floor of Ina reveal a very wide range of individual mound volumes between 41 and 9.2×10^6 m^3 (Qiao et al., 2019), and the mean and median values of 3.0×10^5 and 1.6×10^4 m^3, respectively. In comparison, the 532 RMDSs have mean and median values of 5.3×10^4 and 2.8×10^4 m^3, respectively. Maximum values are around 4.8×10^5 m^3 and minimum values around 540 m^3. All our measurements lie within the range for the Ina mounds as estimated by Wilson and Head (2017a).

Based on the model by Wilson and Head (2017a), the morphology of the mounds is determined by both the rheology and the effusion rate of the magmatic foam. The high viscosity (500 Pa s, compared to 0.5 Pa s for lunar basaltic magma) and the low effusion rate of the foam (~0.6 m^3s^{-1}) limit the lateral and axial spreading and lead to the bubble-like shape and steep sides, much as low effusion rate, viscous silicic flows produce dome-like constructs on Earth. The yield strength of the foam and the low gravitational acceleration on the Moon define the thickness of the extruded lava and hence the height of the mounds (slope lower than about ~5°), similar to the analog of large mare domes showing a low topographic relief (slope < 5°) in the lunar maria (Head & Gifford, 1980; Wöhler et al., 2007; Lena et al., 2013). Here we will not consider the foam mound hypothesis in more detail, given that more strong evidence and further tests are required (see Wilson et al., 2019 for details).

4.5 Implications for the Formation of Ring Moats

The moats around the RMDSs, partly filled with lava flows, are possibly the result of flexing of the underlying flow crust under the load of the mounds and the space created by the extrusion of the still-hot lava out onto the surface. The viscoelasticity of the flow crust could lead to a bending of the crust in response to a vertical force exerted on it. This property could help to explain the structure of the ring moats surrounding lunar RMDSs. This can be visualized from the analogy of the deformation of the rigid lithosphere on Earth. The elastic lithosphere is more likely to relax stresses in its lower, hotter part caused by solid-state creep processes due to hydrostatic equilibrium (Turcotte & Schubert, 2014). The load added on the lithosphere will allow it to bend. The load resulting from the presence of a volcanic island provides strong evidence for this hypothesis, though this analog occurs on a much larger scale than RMDSs. For example, the lithosphere around the Hawaiian Islands is bent downwards as a result of their load, leading to a surrounding area of increased ocean depth (Turcotte & Schubert, 2014). For a moving basaltic lava, the layers from the uppermost crust to the lava core can be divided into brittle crust, visco-elastic crust, and liquid lava (Self et al., 1998). When the lunar RMDSs began to form, the temperature of the flow crust increased with depth and the brittle crust generally thickened with time. The colder crust rocks became sufficiently dense as a result of thermal contraction. The further load of extrusive RMDS via cracks in the upper crust (Wilson et al., 2019; Zhang et al., 2017) made the crust heavy enough to be gravitationally unstable, such that the crust underneath the RMDSs was able to flex downward, potentially forming the pattern of the mounds surrounded by moat structures. Besides, in this interpretation, the withdrawal and discharge of underlying gas-pressured magmas could also help produce voids of variable size below them, further favoring the generation of subsidence of load and moat formation.

4.6 Outstanding Issues Regarding the Origin of RMDSs

The RMDS-crater overlapping stratigraphic relationships are important for establishing the age relationships of RMDSs to the subjacent lunar mare unit. Basilevsky et al. (2019) point out that the degradation ages of the craters on which some RMDSs appear superposed represent a wide range of degradation ages (Basilevsky, 1976) and that the stratigraphically overlapping RMDSs would imply an age of emplacement unrelated to the age of the subjacent maria, but instead imply a very wide range of ages, all subsequent (in many cases by many hundreds of millions of years) to the subjacent mare unit.

Such examples of young morphologic and morphometric characteristics would support Copernican-aged (<1000 Ma) basaltic mare volcanism for the specific RMDSs showing these relationships. For example, Figure 8 presents two cases in which RMDSs appear to be superposed on adjacent craters. The diameter (D) and depth (d) of both craters superposed by RMDSs in Figures 8a and 8b are ~300 m and ~15 m respectively, resulting in a d/D ~0.05 with a maximum steepness of the inner slope α ~9°. This morphometric-morphologic-type crater belongs to morphologic class C of Basilevsky (1976), corresponding to an age between 750 and 1500 Ma (Basilevsky et al., 2019). The crater in Fig. 2 of Basilevsky et al. (2019) is ~115 m in diameter with a shallow depth of 4 m, d/D of 0.035 and α about 6-8°. Its estimated age using the Basilevsky (1976) relationships is interpreted to be in the range of ~140-280 Ma. Therefore, the RMDSs that superposed these craters should be younger than these age values.

The RMDS-superposed craters display distinctive and well-preserved topographic profiles that are the same as common impact structures in a large range of geological settings (Fassett & Thomson, 2014). Several authors have concluded that craters smaller than 300 m are eroded and degraded beyond recognition or are reduced to only ~7% or less of their initial depths, as inferred from characterizing the degradation of small impact craters using a topographic diffusion model (Fassett & Thomson, 2014). Some craters overlapped by RMDSs are so small (some even less than ~150 m diameter) that they cannot have retained their morphologies for up to 3 Ga, the youngest age of the mare units in which the RMDSs are found. These relationships would therefore imply a young age of less than at least 0.5 Ga for these RMDSs. Given that there are mare units in Oceanus Procellarum that have an estimated age of ~1.2 Ga (Hiesinger et al., 2011), the occurrence of small-scale eruptions occurring more recently than 1.0 Ga cannot be ruled out.

Further, during the period with a duration as long as the mean age of lunar maria (~3.5 Ga, Hiesinger et al., 2011) the lunar surface should have been reworked by impact bombardment to form a regolith to an average depth of at least 4-5 m (Bart et al., 2011; McKay et al., 1991; Shkuratov & Bondarenko, 2001), and any pre-existing features (lava flow fronts, tumuli, collapse pits, etc.) up to several meters high (as most of RMDSs are) should have been destroyed beyond recognition. Larger features (for example, impact craters) have their elevation reduced, and morphology smoothed, with a loss of morphological sharpness (e.g., Craddock & Howard, 2000; Fassett & Thomson, 2014; Soderblom, 1970). According to the diffusional degradation hypothesis (e.g. Fassett & Thomson, 2014), RMDSs could have developed and retained their present characteristics in the last 1 Ga only if the cumulative cratering flux was an order of magnitude smaller in the last 3.5 Ga (e.g., Hartmann et al., 2007, their Fig. 4). These relationships provide independent evidence that despite their close compositional and areal similarity to, and association with the background maria on which they occur, the RMDS may have formed completely independently of the background maria at times over a billion years later, and that they continued to form periodically throughout more recent periods of lunar history.

Based on this evidence, and following these lines of reasoning, RMDSs can be interpreted to have formed throughout lunar history after the emplacement age of the host mare basalt units on which they are located. This correlation implies that RMDS formation and emplacement mechanisms must be able to account for the emplacement of very small volumes of lava, of similar composition, at different times in later lunar history. However, the hypothesis that some RMDSs formed independently of the host lava flows on which they are superposed, or that some RMDS clusters, including these partially superposed on or extending into small impact craters, formed during the Copernican Period, present significant challenges to our current understanding of lunar thermal evolution (e.g., Laneuville et al., 2018; Shearer et al., 2006; Ziethe et al., 2009).

The composition of these apparently young RMDSs is of medium to high titanium content (see Section 3.2) and is indistinguishable from the mare materials where they are located, which mainly formed 3 Ga ago (Hiesinger et al., 2011). This requires an explanation of how a much later phase mantle melting could occur, propagating dikes from the deep mantle and delivering magma of the same composition in very small quantities, many times, often separated by hundreds of millions of years (e.g., Wilson & Head, 2017b; Head & Wilson, 2017). Their compositional similarities and co-location suggest that they should have had a similar source depth to the subjacent host maria units. An increase in depth of melting due to the Moon's global conductive cooling with time suggests, however, that the source regions must be in the deep mantle, over several hundred km (>500 km; Solomon & Head, 1979, 1980). It seems unlikely that such source regions could remain active (or were reactivated) over 3 billion years, and also produced and erupted only tiny volumes of somewhat viscous magma (the convex-upward shape of the RMDSs suggests that they could be more viscous than the background maria, despite their similar mineralogy). A major question is how such small volumes of melt could avoid conductive cooling and solidification during transport from the deep mantle through a temporally thickening lithosphere (e.g., Wilson & Head, 2017b; Head &

Wilson, 2017).

There are also unresolved issues related to the rheology of the RMDS lava. The RMDSs are circular or very slightly elongate mounds. They do not have very lobate or extended margins and so the magma that formed them did not flow onto the surface in a manner controlled mainly by the local slope onto which it erupted. Their emplacement was thus likely to be controlled by the inherent magma rheology – their dome-like shape nature implies that the magma was a more viscous fluid with a yield strength that formed domes, which grew mainly as a result of the evolving topographic shape of the dome itself. Yet the composition derived from spectroscopy suggests a basaltic mineralogy (Zhang et al., 2017). Thus, either the magma was very cool when it reached the surface, or it was highly viscous for some other reasons. If cooling was the control factor, cooling could be maximized by the magma moving toward the surface through a narrow pathway (dike) at a slow speed to allow efficient heat loss to the surrounding rock. This is the exact opposite of the requirement of a wide pathway and rapid magma rise to minimize chemical interaction with the surrounding rocks. If one accepts that a wide pathway and rapid rise is essential to explain the uncontaminated chemistry, then the very young eruption of such small and morphologically distinct dome structures requires an extremely fine balance of driving pressure, magma volume and source depth to permit the magma to travel rapidly to the surface, but then erupt only a very small volume. Another difficulty with geologically very young ages for RMDS is how to account for the origin of the topographic moat surrounding the mound. Loading of such individual small volumes seems unlikely to cause flexure of the rigid mare substrate emplaced several 10^9 years ago to form such ring depressions with depths of up to several meters and tens to more than one hundred meters in width.

Therefore, we are faced with a conundrum: On the one hand, the mineralogic and locational similarity of RMDS occurrences and their underlying mare units suggest that they formed by processes associated with the emplacement of the lava and its cooling (Wilson et al., 2019) several billion years ago. On the other hand, stratigraphic relationships of RMDSs and a range of crater degradation ages for craters superposed on the maria, as well as regolith development models, both suggest that the RMDSs were emplaced periodically in the last several hundreds of millions of years, despite challenges to thermal evolution and volcanological emplacement models. Future areas of research to address or resolve these conflicting interpretations might involve: 1) reassessing global thermal evolution models, 2) revisiting models of magma generation, ascent and eruption, 3) reassessing regolith development models and rates, 4) reassessing crater degradation and feature degradation diffusional models, 5) comparison of RMDS formation models to other features of volcanological origin interpreted by some to be of comparable young ages to RMDSs (e.g., Irregular Mare Patches; Braden et al., 2014; Qiao et al. 2019).

5. Summary, Conclusions and Outstanding Questions

1. Synthesis of Observations and New Findings:

Our extensive survey of ring-moat dome structures (RMDSs), positive morphologic features found clustered across many mare regions on the Moon, has extended knowledge of RMDS distribution from the few isolated examples previously reported, to much broader areas of the lunar nearside and farside maria. We have expanded the known number of RMDSs from ~2600 to over 8,000, illustrating that RMDSs are more common geological features than previously thought. Furthermore, we completed a detailed geomorphological analysis of 532 RMDSs identified in several mare basins. This combination of detailed compositional mapping, morphological and morphometric analyses, and spatial distribution relationships with other geologic structures shows that (1) RMDSs represent low circular mounds with diameters of a few hundred meters (average about 200 m) and a mean height of 3.5 m. The mounds are surrounded by moats ranging from tens to over one hundred meters in width and up to several meters in depth; (2) there is a wide variation of titanium abundances, although RMDSs are more commonly found in mare regions of moderate-to-high titanium content (> 3 wt% TiO_2); (3) RMDSs are found to occur on or around fractures, graben and volcanic edifices (small shields and cones); and (4) a spatial association between RMDSs and IMPs (Irregular Mare Patches, identified by Braden et al., 2014) is observed, suggesting that both may form from related lava flow emplacement processes.

More detailed quantitative measurements of 532 RMDSs from various mare basins show that their diameters cover a broad range from 68 to 645 meters. The average diameter is 209 m, and the median 192 m. RMDS heights are from < 1 m to 13.4 meters, with a mean height of 3.6 m and a median height of 3.4 m. RMDSs and Ina mounds are comparable as regards their volumes and presence of geomorphologic moats. Overall, RMDS SFD (Size-Frequency Distribution) differences can be expressed in terms of h/D morphologic trends, with a median of 0.02 (4/200) but with populations skewed towards higher ratio values in the sequence Procellarum-Fecunditatis-Tranquillitatis. These relationships are expressed numerically in the correlation indexes for the wider bins (P-F, 0.94; F-T, 0.86; P-T, 0.64). These trends could reflect differences in the properties of lavas forming RMDSs in individual mare basins, e.g., their composition, viscosity, emplacement style, and source region depth.

Based on M^3 spectral data calibrated to Lunar Prospector Gamma Ray Spectrometer Ti abundance data (Prettyman et al., 2001), twelve measured RMDS sites are located in basaltic regions of relatively high Ti content, between ~5 and 6 wt% TiO_2 on average; the highest RMDS concentrations found in the lunar maria have about ~8 wt% TiO_2. The other elemental abundances (CaO, Al_2O_3, FeO, MgO) indicate typical mare composition for lava flows containing RMDSs. We conclude that RMDSs may form preferentially in maria of moderate to high Ti content. Models of RMDS generation and evolution should take these observations and correlations into account.

Data from our survey on the age and mode of formation of RMDSs is ambiguous and inconclusive. On the one hand, an intimate areal association of RMDSs with their host mare basalt deposits, and lack of any albedo or compositional differences suggests an RMDS origin associated with the emplacement and cooling of the host lava flows 3-4 Ga ago. On the other hand, RMDS embayment relationships with degraded craters superposed on the host lava flow unit, the estimated ages of these degraded craters, and the fact that regolith thicknesses should have obscured the subtle dome and moat topography if formed 3-4 Ga ago, suggest that the RMDSs are young, emplaced in the last 1-3 Ga. We outline these different modes of formation and contradictory age relationships below.

2. Theories for Ring-Moat Dome Structure Origin and Ages:

Class 1 Theories for RMDS Formation: Temporally Associated with Host Lava Flow Emplacement and Cooling: This class of theories for RMDS origin notes the identical mineralogical and geochemical properties of the RMDSs and their host mare basalts, and the intimate areal association (within and surrounded by) the host mare basalts. Based on these associations, theories in this class explore terrestrial analogs and physical volcanological models accounting for lunar conditions, to assess possible origins related to processes associated with lava flow emplacement and cooling.

a) Lava Flow Emplacement Terrestrial Analogs: These explanations look to terrestrial analogs of flood basalts and inflated flows to assess the possibility that RMDSs represent different manifestations of deformation of the upper chilled flow layer, extrusion of lava from the core, internal drainage of lava in the evolving flow, and draping and deformation of the crust, combined in several mechanisms (e.g., squeeze-ups, drainage and draping, tumuli formation, etc.) to produce the RMDS features.

b) Lava Flow Emplacement and Cooling in the Lunar Environment: These explanations assess processes of basaltic lava flow emplacement and cooling in the low-gravity vacuum conditions of the Moon and call on the recent discovery and understanding of the role of H_2O and other volatile species in the sequential degassing and emplacement of lunar lava flows. These treatments predict late-stage flow inflation by vesicular lavas, and subsequent further degassing of lavas by second boiling as the flow cools; the vertical movement of the resulting extremely vesicular and buoyant lava, combined with deformation of the chilled crust by inflation and expansion, results in the cracking of the chilled crust and extrusion of the highly vesicular lavas and magmatic foams to form the RMDSs, all contemporaneous with lava flow emplacement and cooling.

These theories are favored by being able to explain the formation of RMDSs in association with their compositionally similar and intimately areally associated host lava flows. They are seriously contradicted, however, by the following observations:

1) Stratigraphic embayment observations interpreted to mean that some RMDSs formed after the formation of regolith deposits, significantly after the emplacement and cooling of the host lava flows.

2) The very young and multiple ages of degraded impact craters embayed by some RMDSs, suggesting that RMDS emplacement occurred over a long period (>3 Ga) following the emplacement of the host lava flows.

3) The fact that regolith development models predict that lava flows emplaced during the period of peak mare volcanism, ~3-4 Ga, should have a thickness of at least 4-5 m of superposed, impact-induced regolith, a thickness that exceeds the topographic expression of many RMDS mounds and moats. Thus, the current topographic expression of RMDSs implies that they formed in much more recent lunar history, long after emplacement of the host mare basalt units.

Class 2 Theories for RMDS Formation: Temporally Unassociated with Host

Lava Flow Emplacement and Cooling: This class of theories for RMDS origin calls on the three lines of evidence for the young age of RMDS discussed above, and seeks to explain RMDS origin with mechanisms that are unassociated with either the emplacement and cooling of the host lava flows, or the period of peak mare volcanism (3-4 Ga). Stratigraphic and embayed degraded crater relationships are interpreted to mean that RMDS emplacement was episodic, and continued over the last 1-2 Ga, with individual embayed crater degradation ages of hundreds of millions to over a billion years. Regolith development models would favor RMDS formation ages in the last 1-2 Ga, when impact fluxes had waned and regolith thickness predictions are less than the currently observed topographic manifestation of RMDS domes and moats.

Specific volcanological mechanisms for the formation of RMDSs long after the 3-4 Ga peak volcanic flux have not yet been put forth in detail, but young RMDS emplacement mechanisms may share characteristics with those for Irregular Mare Patches (IMPs) (Braden et al., 2014). These IMP features not only contain dome-like mounds, often with surrounding moats, but the three major IMP occurrences (Ina, Sosigenes and Cauchy 5) have also been dated by CSFD measurements to be unassociated with adjacent 3-4 Ga lavas, and to be less than 100 Ma old. As for RMDS ages discussed above, the young CSFD ages of the three major IMP occurrences have found support in linear diffusion regolith development models, which suggest that the ages of specific elements of Ina IMP feature topography (moats, mounds) are less than 100 Ma (Fassett & Thomson, 2015). Braden et al. (2014) suggest a two-stage basalt emplacement model to account for the young emplacement of the Ina mound and floor units, stressing that such very recent mare basalt emplacement requires a reexamination of current lunar thermal evolution models, which predict the decline and cessation of interior melting and basalt emplacement over the last 2 Ga. Schultz et al. (2006) called on late-stage volatile venting at Ina to account for similar observations of the unusual floor and mound units and their young ages.

Mechanisms of RMDS emplacement that are not temporally associated with host lava flow emplacement and cooling are favored by the three lines of evidence for RMDS young ages, and RMDS similarities to Irregular Mare Patches in formation time and in some morphological aspects. The lack of a specific model for the generation, ascent and eruption of late-stage basalts to produce RMDSs of such young ages precludes further assessment of this class of RMDS formation theories. However, on the basis of the

RMDS characterization outlined in this study, we can list the specific elements that any theory should consider. These observations include:

1) Modes of occurrence and associations: Young RMDSs share albedo and compositional characteristics of their ancient host mare materials, occur in most of the major mare deposits, both on the nearside and farside. This implies that the composition of the source regions is likely to be similar to that of the ancient host basalt units. No RMDSs have yet been detected in the highlands.

2) Individual morphology and morphometry: Volcanological emplacement model eruption events need to account for the small volume of the domes, the magma viscosity implied by their slopes, and the formation of the surrounding moats. They also need to account for the typical relatively close-packing and shoulder-to-shoulder distribution, rather than stacking or multiple superposition relationships which are typically not observed.

3) Ages: Individual RMDS occurrences in degraded craters have been dated ranging over a wide spectrum of ages, from hundreds of Ma to 1-2 Ga; this implies that magma emplacement mechanism was active over this period and requires the development of new lunar thermal evolution models to account for this behavior. Elements of these models require maintenance of mantle temperatures sufficiently high to permit the generation, ascent and eruption of magma that was of similar composition to RMDS peak mare basalt host units but was erupted in very much smaller quantities to form individual RMDSs.

4) Modes of eruption: Volcanological emplacement models should account for the small RMDS volumes and distinctive features (domes and associated moats), the episodic emplacement of small lava volumes over several billion years following the host unit emplacement, the compositional similarities to the host unit, the lack of detection in the highlands, and the distinctive clustering and spacing of RMDSs documented in this study. Modes of eruption called upon to explain the other proposed examples of very youthful lunar volcanism, the Irregular Mare Patches (Braden et al., 2014), should be studied for potential insights into RMDS emplacement processes.

3. Recommendations for future exploration and analysis:

The contrasting and contradictory interpretations for RMDS age, origin and evolution outlined above could be resolved by future research and exploration and we outline several promising areas:

1) Ages of the RMDSs and host unit: Individual RMDSs are too small to be dated effectively with CSFD techniques, but any in situ or returned sample radiometric age measurements would quickly resolve the age of their emplacement relative to their host basalt unit. In the meantime, other remote sensing and CSFD measurement techniques (e.g., buffered crater counts, collective RMDS crater counts, improved understanding of small-crater CSFDs, etc.) should be explored to refine CSFD age estimates.

2) Physical properties of the RMDS substrate and host unit: Some theories of RMDS origin temporally associated with host lava flow emplacement and cooling call on the extrusion of highly vesicular lavas and magmatic foams to form the RMDSs. These theories can be further tested with observations comparing the nature of the physical properties and response to subsequent impacts of such vesicular foamy lavas and the surrounding lavas.

3) Improved understanding of impact cratering processes in porous substrates: Current theoretical and experimental data on impact cratering energy partitioning suggest that impacts into very vesicular lavas and magmatic foams will partition significant energy into compression and crushing of the vesicular substrate at the expense of brittle deformation and lateral ejection. Improved understanding of these processes from both theoretical modeling and high-velocity laboratory impact experiments will enhance predictions of superposed crater morphology and morphometry in solid basalt and vesicular/foamy substrates, permitting the better distinction between competing RMDS models.

4) Further constraints from regolith evolution models: Improved understanding of the nature of regolith thickness accretion rates in mare basalt substrates of different ages will help to improve the constraints on RMDS ages required by observed RMDS dome and moat topography. Improved models will also help in the interpretation of regolith thickness estimates from superposed impact crater morphology.

5) Further constraints from evolutionary crater degradation models: This technique is well established, but can the availability of global high-resolution images be used to improve the resolution of the ages of degraded craters to refine estimates of the RMDSs that appear to embay degraded craters?

6) New insights from relations to IMP characteristics and morphology: Could further comparisons of RMDSs and IMPs shed new light on their individual and collective mode

of emplacement and their young ages? Could alternate models for IMP emplacement and ages (compare Braden et al., 2014 and Qiao et al., 2019) be used to help address the disparate theories for RMDS origins?

7) Updated thermal evolution models: Serious attention needs to be paid to revisiting and updating lunar thermal evolution models, to assess ways in which mare volcanism might have extended into the last 2 Ga of lunar history and up to the present.

8) Updated volcanological emplacement models: Current models for the generation, ascent and eruption of basaltic magma on the Moon cannot account for the repeated emplacement of very small volumes of basaltic magma similar in composition to the ancient host basalt over a period of several billion years, up to the geological present. Models should explore and incorporate long-term heat sources, reheating and melting scenarios, segregation and storage of volatiles, and other non-traditional scenarios to see if explanations for observed RMDS characteristics and young ages can be found.

9) Continued documentation of RMDS global distribution and characterization: Our current analysis extends the areal coverage of known RMDSs and their total number of to >8000, >5400 more than our earlier study. The new insights revealed by the current analysis, and the ability to better define competing theories of RMDS origin, strongly suggest that much additional documentation and characterization using existing data and any newly acquired data need to be carried out to address the key questions of RMDS age and origin.

10) Optimizing image viewing geometry for detection and characterization: Images characterized by lower solar illumination geometries revealed the wide distribution and abundance of RMDSs due to their low topography and slopes (e.g., Figure 19). The international armada of lunar orbiting spacecraft should include in their mission planning scenarios acquisition of low to very low sun illumination geometry images and remote sensing data on the mineralogy and physical properties to help complete the global inventory of RMDS characteristics, distributions, associations and modes of occurrence.

11) Future exploration experiments and missions: The enigmatic characteristics and ages of the RMDSs, and their fundamental significance in understanding the thermal and volcanological history of the Moon, mean that RMDS exploration should have a high priority in new remote sensing, landed science, rover science, and robotic sample return missions. The broad development of RMDSs in individual occurrences and their complex relationships make many occurrences ideal landing sites for Apollo-like human

exploration missions and associated geological traverses and geophysical surveys.

Acknowledgments

The LROC NAC data and M^3 reflectance data used in this paper are archived in the Geophysics Node of the Planetary Data System (PDS). The Kaguya TC data were acquired by the JAXA lunar orbiter KAGUYA/SELENE. The data presented in Figures 4, 6, and 7 and all the 8281 RMDSs identified so far across the global Moon and shown in Figure 1 can be found online (https://doi.org/10.5281/zenodo.3370821 and .3711659). The NAC-based DEM data (and all other appropriate data associated with our article) will be available at http://www.bv.e-technik.tu-dortmund.de/cms/de/forschung/Bildsequenzen_und_Referenzdaten/index.html. This manuscript benefited from thoughtful reviews by J.L. Whitten and an anonymous reviewer. FZ was funded by the Science and Technology Development Fund, Macau SAR (131/2017/A3, 0042/2018/A2), and the National Natural Science Foundation of China (11903090, 41590851). YLZ was supported by Beijing Municipal Science and Technology Commission (Grant No. Z181100002918003). We gratefully acknowledge funding to JWH for participation as co-investigator in the LOLA Experiment Team (Grants NNX11AK29G and NNX13AO77G - National Aeronautics and Space Administration - Goddard). Much of the synthesis work for this contribution was enabled by participation in the NASA Solar System Exploration Research Virtual Institute, through the SEEED (SSERVI Evolution and Environment of Exploration Destinations) cooperative agreement number NNA14AB01A at Brown University. LW thanks the Leverhulme Trust for support through an Emeritus Fellowship.

Reference

Anderson, S. W., Smrekar, S. E., & Stofan, E. R. (2012). Tumulus development on lava flows: insights from observations of active tumuli and analysis of formation models. *Bulletin of Volcanology*, *74*(4), 931-946.

Arvidson, R., Drozd, R., Hohenberg, C., Morgan, C., & Poupeau, G. (1975). Horizontal transport of the regolith, modification of features, and erosion rates on the lunar surface. *The Moon*, *13*(1-3), 67-79.

Aubele, J. C., Crumpler, L. S., & Elston, W. E. (1988). Vesicle zonation and vertical structure of basalt flows. *Journal of Volcanology and Geothermal Research*, *35*(4), 349-374.

Barker, M., Mazarico, E., Neumann, G., Zuber, M., Haruyama, J., & Smith, D. (2016). A new lunar digital elevation model from the Lunar Orbiter Laser Altimeter and SELENE Terrain Camera. *Icarus*, *273*, 346-355.

Bart, G. D., Nickerson, R. D., Lawder, M. T., & Melosh, H. (2011). Global survey of lunar regolith depths from LROC images. *Icarus*, *215*(2), 485-490.

Basilevsky, A. (1976). On the evolution rate of small lunar craters. In *7th Lunar and Planetary Science Conference*, 1005-1020. The Woodlands, TX.

Basilevsky, A. T., Zhang, F., Wöhler, C., Bugiolacchi, R., Head, J. W., & Wilson, L. (2019). Lunar Ring-Moat Dome Structures and Their Relationships with Small Impact Craters. In *50th Lunar and Planetary Science Conference* (abstract 1507). The Woodlands, TX.

Bernardi, M. I., Bertotto, G. W., Jalowitzki, T. L., Orihashi, Y., & Ponce, A. D. (2015). Emplacement history and inflation evidence of a long basaltic lava flow located in Southern Payenia Volcanic Province, Argentina. *Journal of Volcanology and Geothermal Research*, *293*, 46-56.

Bernardi, M. I., Bertotto, G. W., Ponce, A. D., Orihashi, Y., & Sumino, H. (2019). Volcanology and inflation structures of an extensive basaltic lava flow in the Payenia Volcanic Province, extra-Andean back arc of Argentina. *Andean geology*, *46*(2), 279-299.

Bhatt, M., Mall, U., Wöhler, C., Grumpe, A., & Bugiolacchi, R. (2015). A comparative study of iron abundance estimation methods: Application to the western nearside of the Moon. *Icarus*, *248*, 72-88.

Bhatt, M., Wöhler, C., Grumpe, A., Hasebe, N., & Naito, M. (2019). Global mapping of lunar refractory elements: multivariate regression vs. machine learning. *Astronomy & Astrophysics*, *627*, A155.

Braden, S., Stopar, J., Robinson, M., Lawrence, S., Van Der Bogert, C., & Hiesinger, H. (2014). Evidence for basaltic volcanism on the Moon within the past 100 million years. *Nature Geoscience*, *7*(11), 787-791.

Bresenham, J. E. (1965). Algorithm for computer control of a digital plotter. *IBM Systems Journal, 4*(1), 25-30.

Calvari, S., Neri, M., & Pinkerton, H. (2003). Effusion rate estimations during the 1999 summit eruption on Mount Etna, and growth of two distinct lava flow fields. *Journal of Volcanology and Geothermal Research*, *119*(1-4), 107-123.

Cashman, K. V., & Kauahikaua, J. P. (1997). Reevaluation of vesicle distributions in basaltic lava flows. *Geology*, *25*(5), 419-422.

Chitwood, L. (1994). Inflated basaltic lava—Examples of processes and landforms from central and southeast Oregon. *Oregon Geology*, *56*(1), 11-21.

Craddock, R. A., & Howard, A. D. (2000), Simulated degradation of lunar impact craters and a new method for age dating farside mare deposits. *Journal of Geophysical Research*, *105*, 20, 387–20,401.

Diniega, S., Sangha, S., & Browne, B. (2018). Using satellite imagery to identify and analyze tumuli on Earth and Mars. *Earth and Planetary Science Letters*, *482*, 52-61.

Duncan, A., Guest, J., Stofan, E., Anderson, S., Pinkerton, H., & Calvari, S. (2004). Development of tumuli in the medial portion of the 1983 aa flow-field, Mount Etna, Sicily. *Journal of Volcanology and Geothermal Research*, *132*(2), 173-187.

Duraiswami, R. A., Bondre, N. R., & Dole, G. (2004). Possible lava tube system in a hummocky lava flow at Daund, western Deccan volcanic province, India. *Journal of Earth System Science*, *113*(4), 819-829.

Duraiswami, R. A., Bondre, N., Dole, G., & Phadnis, V. (2002). Morphology and structure of flow-lobe tumuli from Pune and Dhule areas, western Deccan Volcanic Province. *Journal Geological Society of India*, *60*(1), 57-66.

Duraiswami, R. A., Bondre, N. R., Dole, G., Phadnis, V. M., & Kale, V. S. (2001). Tumuli and associated features from the western Deccan Volcanic Province, India. *Bulletin of Volcanology*, *63*(7), 435-442.

Elkins-Tanton, L. T., Burgess, S., & Yin, Q. Z. (2011). The lunar magma ocean: Reconciling the solidification process with lunar petrology and geochronology. *Earth and Planetary Science Letters*, *304*(3-4), 326-336.

Elshaafi, A., & Gudmundsson, A. (2019). Emplacement and inflation of the Al-Halaq al Kabir lava flow field, central part of the Al Haruj Volcanic Province, Central Libya. *Journal of Volcanology and Geothermal Research*, *381*, 284-301.

Ernst, R. E., Head, J. W., Parfitt, E., Grosfils, E., & Wilson, L. (1995). Giant radiating dyke swarms on Earth and Venus. *Earth-Science Reviews*, *39*(1-2), 1-58.

Fa, W., Zhu, M. H., Liu, T., & Plescia, J. B. (2015). Regolith stratigraphy at the Chang'E−3 landing site as seen by lunar penetrating radar. *Geophysical Research Letters*, *42*(23), 10179-10187.

Fassett, C. I., & Thomson, B. J. (2014). Crater degradation on the lunar maria: Topographic diffusion and the rate of erosion on the Moon. *Journal of Geophysical Research: Planets*, *119*(10), 2255-2271.

Frohlich, C., & Nakamura, Y. (2009). The physical mechanisms of deep moonquakes and intermediate-depth earthquakes: How similar and how different?. *Physics of the Earth and Planetary Interiors*, *173*(3-4), 365-374.

Garry, W., Robinson, M., Zimbelman, J., Bleacher, J., Hawke, B., Crumpler, et al. (2012). The origin of Ina: Evidence for inflated lava flows on the Moon. *Journal of Geophysical Research: Planets*, *117*(E12).

Giacomini, L., Massironi, M., Martellato, E., Pasquarè, G., Frigeri, A., & Cremonese, G. (2009). Inflated flows on Daedalia Planum (Mars)? Clues from a comparative analysis with the Payen volcanic complex (Argentina). *Planetary and Space Science*, *57*(5-6), 556-570.

Glaze, L., Anderson, S., Stofan, E., Baloga, S., & Smrekar, S. (2005). Statistical distribution of tumuli on pahoehoe flow surfaces: Analysis of examples in Hawaii and Iceland and potential applications to lava flows on Mars. *Journal of Geophysical Research: Solid Earth*, *110*(B8), B08202.

Greeley, R., & Hyde, J. H. (1972). Lava tubes of the cave basalt, Mount St. Helens, Washington. *Geological Society of America Bulletin*, *83*(8), 2397-2418.

Gregg, T. K. (2017). Patterns and processes: subaerial lava flow morphologies: a review. *Journal of Volcanology and Geothermal Research*, *342*, 3-12.

Grove, T. L., & Krawczynski, M. J. (2009). Lunar mare volcanism: Where did the magmas come from?. *Elements*, *5*(1), 29-34.

Grumpe, A., Belkhir, F., & Wöhler, C. (2014). Construction of lunar DEMs based on reflectance modelling. *Advances in Space Research 53*(12), 1735–1767.

Grumpe, A., Schröer, C., Kauffmann, S., Fricke, T., Wöhler, C., & Mall, U. (2016). Refinement of

Stereo Image Analysis Using Photometric Shape Recovery as an Alternative to Bundle Adjustment. *ISPRS - International Archives of the Photogrammetry, Remote Sensing and Spatial Information Sciences*, Volume XLI-B4, pp.565-572.

Grumpe, A. & Wöhler, C. (2014). Recovery of elevation from estimated gradient fields constrained by digital elevation maps of lower lateral resolution. *ISPRS Journal of Photogrammetry and Remote Sensing 94*, 37–54.

Grumpe, A., Wöhler, C., Rommel, D., Bhatt, M., & Mall, U. (2018). Elemental and topographic mapping of lava flow structures in Mare Serenitatis on the Moon. In: B. Wu, K. Di, J. Oberst, I. Karachevtseva (eds.), Planetary Remote Sensing and Mapping, CRC Press, 2018.

Grumpe, A., Zirin, V., & Wöhler, C. (2015). A normalisation framework for (hyper-)spectral imagery. *Planetary and Space Science 111*, 1-33.

Guest, J. E., Wood, C., & Greeley, R. (1984). Lava tubes, terraces and megatumuli on the 1614–24 pahoehoe lava flow field, Mount Etna, Sicily. *Bulletin Volcanologique*, *47*(3), 635-648.

Hapke, B. (1981). Bidirectional reflectance spectroscopy: 1. Theory. *Journal of Geophysical Research 86*(B4), 3039–3054.

Hapke, B. (1984). Bidirectional reflectance spectroscopy: 3. Correction for macroscopic roughness. *Icarus 59*(1), 41-59.

Hapke, B. (2002). Bidirectional reflectance spectroscopy: 5. The Coherent Backscatter Opposition Effect and Anisotropic Scattering. *Icarus 157*(2), 523-534.

Hartmann, W. K., Quantin, C., & Mangold, N. (2007). Possible long-term decline in impact rates: 2. Lunar impact-melt data regarding impact history. *Icarus*, *186*(1), 11-23.

Haruyama, J., Hara, S., Hioki, K., et al. (2012). lunar global digital terrain model dataset produced from selene (kaguya) terrain camera stereo observations. In *43th Lunar and Planetary Science Conference* (Abstract 1200). The Woodlands, TX.

Haruyama, J., Matsunaga, T., Ohtake, M., Morota, T., Honda, C., Yokota, Y., et al. (2008b). Global lunar-surface mapping experiment using the Lunar Imager/Spectrometer on SELENE. *Earth, planets and space*, *60*(4), 243-255.

Haruyama, J., Ohtake, M., Matsunaga, T., Morota, T., Yokota, Y., Honda, C., et al. (2008a). Planned radiometrically calibrated and geometrically corrected products of lunar high-resolution Terrain Camera on SELENE. *Advances in Space Research*, *42*(2), 310-316.

Hauri, E. H., Weinreich, T., Saal, A. E., Rutherford, M. C., & Van Orman, J. A. (2011). High pre-eruptive water contents preserved in lunar melt inclusions. *Science*, *333*(6039), 213-215.

Head, J. W. (1976). Lunar volcanism in space and time. *Reviews of Geophysics*, *14*(2), 265-300.

Head, J., & Gifford, A. (1980). Lunar mare domes: Classification and modes of origin. *Earth, Moon, and Planets*, *22*(2), 235-258.

Head, J., & Wilson, L. (1993). Lunar graben formation due to near-surface deformation accompanying dike emplacement. *Planetary and Space Science*, *41*, 719-727.

Head, J., & Wilson, L. (2017). Generation, ascent and eruption of magma on the Moon: New insights into source depths, magma supply, intrusions and effusive/explosive eruptions (Part 2: Predicted emplacement processes and observations). *Icarus*, *283*, 176-223.

Hess, P. C. (2000). On the source regions for mare picrite glasses. *Journal of Geophysical Research: Planets*, *105*(E2), 4347-4360.

Hon, K., Kauahikaua, J. Denlinger, R. & Mackay, K. (1994). Emplacement and inflation of pahoehoe sheet flows: Observations and measurements of active lava flows on Kilauea Volcano, Hawaii. *Geological Society of America Bulletin*, *106*(3), 351-370.

Horn, B. K. P. (1990). Height and Gradient from Shading. *International Journal of Computer Vision* *5*(1), 37–75.

Hörz, F., Grieve, R., Heiken, G., Spudis, P., & Binder, A. (1991). Lunar surface processes. In The *Lunar sourcebook*, 61-120, eds. Heiken, G. H. et al., Cambridge Univ. press.

Joy, K. H., Crawford, I. A., Russell, S. S., & Kearsley A. T. (2010). Lunar meteorite regolith breccias: An in situ study of impact melt composition using LA-ICP-MS with implications for the composition of the lunar crust. *Meteoritics & Planetary Science*, *45*(6), 917-946.

Kato, M., Sasaki, S., & Takizawa, Y. (2010). The Kaguya mission overview. *Space science reviews*, *154*(1-4), 3-19.

Kauahikaua, J., Cashman, K. V., Mattox, T. N., Heliker, C. C., Hon, K. A., Mangan, M. T., & Thornber, C. R. (1998). Observations on basaltic lava streams in tubes from Kilauea Volcano, island of Hawai'i. *Journal of Geophysical Research: Solid Earth*, *103*(B11), 27303-27323.

Keszthelyi, L. (2008). Inflated pahoehoe at Rima Hadley. In *39th Lunar and Planetary Science Conference* (Abstract 2339). The Woodlands, TX.

Keszthelyi, L., Jaeger, W., McEwen, A., Tornabene, L., Beyer, R. A., Dundas, C., & Milazzo, M. (2008). High Resolution Imaging Science Experiment (HiRISE) images of volcanic terrains from the first 6 months of the Mars Reconnaissance Orbiter primary science phase. *Journal of Geophysical Research: Planets*, *113*(E4), E04005.

Keszthelyi, L., & Pieri, D. C. (1993). Emplacement of the 75-km-long Carrizozo lava flow field, south-central New Mexico. *Journal of volcanology and geothermal research*, *59*(1-2), 59-75.

Keszthelyi, L., & Self, S. (1998). Some physical requirements for the emplacement of long basaltic lava flows. *Journal of Geophysical Research: Solid Earth*, *103*(B11), 27447-27464.

Keszthelyi, L., McEwen, A., & Thordarson, T. (2000). Terrestrial analogs and thermal models for Martian flood lavas. *Journal of Geophysical Research: Planets*, *105*(E6), 15027-15049.

Khalaf, E. E. D. A. H., & Hammed, M. S. (2016). Morphology and development of pahoehoe flow-lobe tumuli and associated features from a monogenetic basaltic volcanic field, Bahariya Depression, Western Desert, Egypt. *Journal of African Earth Sciences*, *113*, 165-180.

Kirk, R. L. (1987). III A fast finite element algorithm for two-dimensional photoclinometry. Ph.D. Thesis (unpublished), California Institute of Technology, Pasadena.

Klimczak, C. (2014). Geomorphology of lunar grabens requires igneous dikes at depth. *Geology*, *42*(11), 963-966.

Kolzenburg, S., Jaenicke, J., Münzer, U., & Dingwell, D. B. (2018). The effect of inflation on the morphology-derived rheological parameters of lava flows and its implications for interpreting remote sensing data-A case study on the 2014/2015 eruption at Holuhraun, Iceland. *Journal of Volcanology and Geothermal Research*, *357*, 200-212.

Kreslavsky, M. A., Head, J. W., Neumann, G. A., Rosenburg, M. A., Aharonson, O., Smith, D. E., & Zuber, M. T. (2013). Lunar topographic roughness maps from Lunar Orbiter Laser Altimeter (LOLA) data: Scale dependence and correlation with geologic features and units. *Icarus*, *226*(1), 52-66.

Laneuville, M., Taylor, J., & Wieczorek, M. (2018). Distribution of Radioactive Heat Sources and Thermal History of the Moon. *Journal of Geophysical Research. Planets*, *123*(12), 3,144-3,166.

Lena, R., Wöhler, C., Phillips, J., & Chiocchetta. M. T. (2013). Lunar Domes: Properties and Formation Processes. Springer Verlag, Milano, Italy.

Lucey, P. G., Blewett, D. T., & Jolliff, B. L. (2000). Lunar iron and titanium abundance algorithms based on final processing of Clementine ultraviolet-visible images. *Journal of Geophysical Research*, *105*, 20297 – 20305.

Mangan, M. T., & Cashman, K. V. (1996). The structure of basaltic scoria and reticulite and inferences for vesiculation, foam formation, and fragmentation in lava fountains. *Journal of Volcanology and Geothermal Research*, *73*(1), 1-18.

McKay, D. S., Heiken, G., Basu, A, Blanford, G., Simon, S., Reedy, R., French, B. M., Papike, J. (1991). The lunar regolith. In: *Lunar Source Book: A User Guide to the Moon*. G.H. Heiken, D.T. Vaniman, B.M. French eds., Cambridge University Press, 285-356.

Németh, K., Haller, M. J., Martin, U., Risso, C., & Massaferro, G. (2008). Morphology of lava tumuli from Mendoza (Argentina), Patagonia (Argentina), and Al-Haruj (Libya). *Zeitschrift für Geomorphologie*, *52*(2), 181-194.

Nyquist, L. E., & Shih, C. Y. (1992). The isotopic record of lunar volcanism. *Geochimica et Cosmochimica Acta*, *56*(6), 2213-2234.

Ollier, C. D. (1964). Tumuli and lava blisters of Victoria, Australia. *Nature*, *202*(4939), 1,284-1,286.

Orr, T. R., Bleacher, J. E., Patrick, M. R., & Wooten, K. M. (2015). A sinuous tumulus over an active lava tube at Kīlauea Volcano: Evolution, analogs, and hazard forecasts. *Journal of Volcanology and Geothermal Research*, *291*, 35-48.

Pasquarè, G., Bistacchi, A., Francalanci, L., Bertotto, G. W., Boari, E., Massironi, M., & Rossotti, A. (2008). Very long pahoehoe inflated basaltic lava flows in the Payenia Volcanic Province (Mendoza and La Pampa, Argentina). *Revista de la Asociación Geológica Argentina*, *63*(1), 131-149.

Pieters, C. M., Boardman, J., Buratti, B., Chatterjee, A., Clark, R., Glavich, T., Green, R., Head, J., Isaacson, P., & Malaret, E. (2009). The Moon Mineralogy Mapper (M^3) on Chandrayaan-1. *Current Science*, *96*(4), 500-505.

Poulet, F., Cuzzi, J., Cruikshank, D., Roush, T., & Dalle Ore, C. (2002). Comparison between the Shkuratov and Hapke scattering theories for solid planetary surfaces: Application to the surface composition of two Centaurs. *Icarus*, *160*(2), 313-324.

Qiao, L., Head, J. W., Wilson, L., & Ling, Z. (2020). The Cauchy 5 Small, Low-Volume Lunar Shield Volcano: Evidence for Volatile Exsolution-Eruption Patterns and Type 1/Type 2 Hybrid Irregular Mare Patch (IMP) Formation. *Journal of Geophysical Research: Planets*, *125*(2), e2019JE006171.

Qiao, L., Head, J. W., Ling, Z., Wilson, L., Xiao, L., Dufek, J. D., & Yan, J. (2019). Geological Characterization of the Ina Shield Volcano Summit Pit Crater on the Moon: Evidence for Extrusion of Waning‐Stage Lava Lake Magmatic Foams and Anomalously Young Crater Retention Ages. *Journal of Geophysical Research: Planets*, *124*(4), 1100-1140.

Qiao, L., Head, J. W., Wilson, L., Xiao, L., Kreslavsky, M., & Dufek, J. (2017). Ina pit crater on the Moon: Extrusion of waning-stage lava lake magmatic foam results in extremely young crater retention ages. *Geology*, *45*(5), 455-458.

Qin, C., Muirhead, A. C., & Zhong, S. (2012). Correlation of deep moonquakes and mare basalts: Implications for lunar mantle structure and evolution. *Icarus*, *220*(1), 100-105.

Rader, E., Vanderkluysen, L., & Clarke, A. (2017). The role of unsteady effusion rates on inflation in long-lived lava flow fields. *Earth and Planetary Science Letters*, *477*, 73-83.

Robinson, M., Brylow, S., Tschimmel, M., Humm, D., Lawrence, S., Thomas, P., et al. (2010). Lunar reconnaissance orbiter camera (LROC) instrument overview. *Space Science Reviews*, *150*(1), 81-124.

Rosenburg, M. A., Aharonson, O., Head, J. W., Kreslavsky, M. A., Mazarico, E., Neumann, G. A., et al. (2011). Global surface slopes and roughness of the Moon from the Lunar Orbiter Laser Altimeter. *Journal of Geophysical Research: Planets*, *116*, E02001.

Rossi, M., & Gudmundsson, A. (1996). The morphology and formation of flow-lobe tumuli on Icelandic shield volcanoes, *Journal of Volcanology and Geothermal Research*, *72*(3-4), 291-308.

Saal, A. E., Hauri, E. H., Cascio, M. L., Van Orman, J. A., Rutherford, M. C., & Cooper, R. F. (2008). Volatile content of lunar volcanic glasses and the presence of water in the Moon’s interior. *Nature*, *454*(7201), 192-195.

Sato, H., Robinson, M. S., Lawrence, S. J., Denevi, B. W., Hapke, B., Jolliff, B. L., & Hiesinger, H. (2017). Lunar mare TiO_2 abundances estimated from UV/Vis reflectance. *Icarus*, *296*, 216-238.

Savage, W. Z. (1978). The development of residual stress in cooling rock bodies. *Geophysical Research Letters*, *5*(8), 633-636.

Schaber, G. G. (1973). Lava flows in Mare Imbrium: Geologic evaluation from Apollo orbital photography. In *4th Lunar and Planetary Science Conference* (p.73-92). The Woodlands, TX.

Scholten, F., Oberst, J., Matz, K. D., Roatsch, T., Wählisch, M., Speyerer, E. J., & Robinson, M. S. (2012). GLD100: The near−global lunar 100 m raster DTM from LROC WAC stereo image data. *Journal of Geophysical Research: Planets*, *117*(E12), E00H17.

Schultz, P., & Greeley, R. (1976). Ring-moat structures: preserved flow morphology on Lunar Maria. In *7th Lunar and Planetary Science Conference* (p. 788-789). The Woodlands, TX.

Schultz, P., Greeley, R., & Gault, D. (1976). Degradation of small mare surface features. In *7th Lunar and Planetary Science Conference* (p. 985-1003). The Woodlands, TX.

Self, S., Keszthelyi, L., & Thordarson, T. (1998). The importance of pāhoehoe. *Annual Review of Earth and Planetary Sciences*, *26*(1), 81-110.

Self, S., Thordarson, T., & Keszthelyi, L. (1997). Emplacement of continental flood basalt lava flows. In: Mahoney, J. J., Coffin, M. F. (Eds.), *Large Igneous Provinces: continental, oceanic, and planetary flood volcanism*. In: Geophys. Monogr., *100*, 381-410.

Self, S., Thordarson, T., Keszthelyi, L., Walker, G. P. L., Hon, K., Murphy, M. T., Long, P., & Finnemore, S. (1996). A new model for the emplacement of Columbia River basalts as large, inflated pahoehoe lava flow fields. *Geophysical Research Letters*, *23*(19), 2689-2692.

Shearer, C. K., Hess, P. C., Wieczorek, M. A., et al. (2006). Thermal and Magmatic Evolution of the Moon. *Reviews in Mineralogy & Geochemistry*, *60*, 365-518.

Shkuratov, Y., Starukhina, L., Hoffmann, H., & Arnold, G. (1999). A model of spectral albedo of particulate surfaces: Implications for optical properties of the moon. *Icarus*, *137*(2), 235-246.

Shkuratov, Y., & Bondarenko, N. (2001). Regolith layer thickness mapping of the Moon by radar and optical data. *Icarus*, *149*(2), 329-338.

Smith, D. E., Zuber, M. T., Neumann, G. A., Lemoine, F. G., Mazarico, E., Torrence, M. H., ... & Aharonson, O. (2010). Initial observations from the lunar orbiter laser altimeter (LOLA). *Geophysical Research Letters*, *37*(18), L18204.

Soderblom, L. A. (1970). A model for small-impact erosion applied to the lunar surface, *Journal of Geophysical Research*, *75*, 2,655–2,661.

Solomon, S. C., & Head, J. W. (1979). Vertical movement in mare basins: Relation to mare emplacement, basin tectonics, and lunar thermal history. *Journal of Geophysical Research: Solid Earth*, *84*(B4), 1,667-1,682.

Solomon, S. C., & Head, J. W. (1980). Lunar mascon basins: Lava filling, tectonics, and evolution of the lithosphere. *Reviews of Geophysics*, *18*(1), 107-141.

Spudis, P. D., McGovern, P. J., & Kiefer, W. S. (2013). Large shield volcanoes on the Moon. *Journal of Geophysical Research: Planets*, *118*(5), 1063-1081.

Stephenson, P. J., Burch‐Johnston, A. T., Stanton, D., & Whitehead, P. W. (1998). Three long lava flows in north Queensland. *Journal of Geophysical Research: solid earth*, *103*(B11), 27359-27370.

Swanson, D. A. (1973). Pahoehoe flows from the 1969–1971 Mauna Ulu eruption, Kilauea volcano, Hawaii. *Geological Society of America Bulletin*, *84*(2), 615-626.

Thordarson, T., & Self, S. (1998). The Roza Member, Columbia River Basalt Group: A gigantic pahoehoe lava flow field formed by endogenous processes?. *Journal of Geophysical Research: Solid Earth*, *103*(B11), 27411-27445.

Turcotte, D., & Schubert, G. (2014). *Geodynamics*, Cambridge University Press, p. 7-8.

Tye, A., & Head, J. W. (2013). Mare Tranquillitatis: Distribution of mare domes, relation to broad mare rise, and evidence of a previously unrecognized basin from LOLA altimetric data. In 44th *Lunar and Planetary Science Conference* (abstract 1319). The Woodlands, TX.

Wagner, R. V., Speyerer, E. J., Robinson, M. S., and LROC Team (2015). New Mosaicked Data Products from the LROC Team. In 46th *Lunar and Planetary Science Conference* (abstract 1473). The Woodlands, TX.

Walker, G. P. (1991). Structure, and origin by injection of lava under surface crust, of tumuli,“lava rises”,“lava-rise pits”, and “lava-inflation clefts” in Hawaii. *Bulletin of Volcanology*, *53*(7), 546-558.

Warell, J. (2004). Properties of the Hermean regolith: IV. Photometric parameters of Mercury and the Moon contrasted with Hapke modelling. *Icarus, 167*(2), 271-286.

Warren P. H. (1994). Lunar and Martian meteorite delivery systems. *Icarus*, *111*, 338-363.

Williams, D. A., Fagents, S. A., & Greeley, R. (2000). A reassessment of the emplacement and erosional potential of turbulent, low‐viscosity lavas on the Moon. *Journal of Geophysical Research: Planets*, *105*(E8), 20189-20205.

Weitz, C., & Head, J. (1999). Spectral properties of the Marius Hills volcanic complex and implications for the formation of lunar domes and cones. *Journal of Geophysical Research: Planets*, *104*(E8), 18,933-18,956.

Wentworth, C. K., & Macdonald, G. A. (1953). Structures and forms of basaltic rocks in Hawaii. US Govt. Print. Off., U.S. Geol. Surv Bull.

Whitford‐Stark, J. L., & Head, J. W. (1980). Stratigraphy of Oceanus Procellarum basalts: Sources and styles of emplacement. *Journal of Geophysical Research: Solid Earth*, *85*(B11), 6579-6609.

Whitten, J. L., & Head, J. W. (2015). Lunar cryptomaria: Physical characteristics, distribution, and implications for ancient volcanism. *Icarus*, *247*, 150-171.

Wilhelms, D. E. (1972). Geologic Map of the Tarunitius Quadrangle of the Moon. Technical Report. U.S. Geol. Survey Map I-722.

Wilhelms, D. E., John, F., & Trask, N. J. (1987). The geologic history of the Moon.*U.S. Geological Survey Professional Paper* 1348. US. Government Printing Office, Washington, DC, p. 85-103.

Wilson, L., & Head, J. (2017a). Eruption of magmatic foams on the Moon: Formation in the waning stages of dike emplacement events as an explanation of “irregular mare patches”. *Journal of Volcanology and Geothermal Research*, *335*, 113-127.

Wilson, L., & Head, J. (2017b). Generation, ascent and eruption of magma on the Moon: New insights into source depths, magma supply, intrusions and effusive/explosive eruptions (Part 1: Theory). *Icarus*, *283*, 146-175.

Wilson, L., & Head, J. (2018). Controls on Lunar Basaltic Volcanic Eruption Structure and Morphology: Gas Release Patterns in Sequential Eruption Phases. *Geophysical Research Letters*, *45*(12), 5852-5859.

Wilson, L., Head, J., & Zhang, F. (2019). A Theoretical Model for the Formation of Ring Moat Dome Structures: Products of Second Boiling in Lunar Basaltic Lava Flows. *Journal of Volcanology and Geothermal Research*, *374*, 160-180.

Wöhler, C., Grumpe, A., Berezhnoy, A., & Shevchenko, V. (2017). Time-of-day–dependent global distribution of lunar surficial water/hydroxyl. *Science advances*, *3*(9), e1701286.

Wöhler, C., Grumpe, A., Berezhnoy, A., Bhatt, M., & Mall, U. (2014). Integrated topographic, photometric and spectral analysis of the lunar surface: Application to impact melt flows and ponds. *Icarus*, *235*, 86-122.

Wöhler, C., Lena, R., & Phillips, J. (2007). Formation of lunar mare domes along crustal fractures: Rheologic conditions, dimensions of feeder dikes, and the role of magma evolution. *Icarus*, *189*(2), 279-307.

Wood, C., Higgins, W., Pau, K., & Mengoli, G. (2005). The Lamont-Gardner Megadome alignment: a lunar volcano-tectonic structure?. In *36th Lunar and Planetary Science Conference* (abstract 1116). The

Woodlands, TX.

Zhang, F., Head, J., Basilevsky, A., Bugiolacchi, R., Komatsu, G., Wilson, L., Fa, W., & Zhu, M. (2017). Newly Discovered Ring‐Moat Dome Structures in the Lunar Maria: Possible Origins and Implications. *Geophysical Research Letters*, *44*(18), 9216-9224.

Zhang, F., Wöhler, C., Head, J. W., Bugiolacchi, R., Wilson, L., & Grumpe, A. (2018a). Ring-Moat Dome Structures (RMDS) in the lunar maria: further statistical and morphological characterization. In *49th Lunar and Planetary Science Conference* (abstract 1374). The Woodlands, TX.

Zhang, F., Zhu, M. H., & Zou, Y. L. (2016). Late stage Imbrium volcanism on the Moon: Evidence for two source regions and implications for the thermal history of Mare Imbrium. *Earth and Planetary Science Letters*, *445*, 13-27.

Zhang, F., Zhu, M. H., Bugiolacchi, R., Huang, Q., Osinski, G. R., Xiao, L., & Zou, Y. L. (2018b). Diversity of basaltic lunar volcanism associated with buried impact structures: Implications for intrusive and extrusive events. *Icarus*, *307*, 216-234.

Ziethe, R., Seiferlin, K., & Hiesinger, H. (2009). Duration and extent of lunar volcanism: Comparison of 3D convection models to mare basalt ages. *Planetary and space science*, *57*(7), 784-796.

Table 1 Summary of the twelve small regions of interest, used NAC frames, and the total number of RMDSs measured in each region. Their locations are marked by the yellow boxes in Figure 2.

Area	**Longitude (West, East)**	**Latitude (North, South)**	**Host Mare**	**Pair NAC frame IDs**	**Num of RMDSs**
A1	30.62, 30.98	10.57, 9.94	Tranquillitatis	M1096293859LE and RE	106
A2	27.30, 27.63	6.30, 5.53		M1172873803LE and RE	50
A3	29.90, 30.30	7.62, 6.84		M1111613936LE and RE	40
A4	-37.42, -37.15	-22.60, -23.23	Humorum	M1142680981 LE and RE	6
A5	52.65, 52.99	0.32, -0.41	Fecunditatis	M180822975 LE and RE	24
A6	52.04, 52.33	-1.07, -1.50		M1142098334LE and RE	26
A7	52.31, 52.68	-1.09, -1.92		M1126787189LE and RE	56
A8	55.76, 55.89	0.22, -0.62		M131284180LE and RE	40
A9	-44.04, -43.75	-9.61, -9.90	Oceanus Procellarum	M1158041551 LE and RE	17
A10	-43.53, -43.25	-9.53, -11.04		M1154499450 LE and RE	80
A11	-43.34, -43.07	-9.56, -10.72		M1173335389 LE and RE	60
A12	-43.75, -43.60	-10.22, -10.84		M162595520 LE and RE	27

Table 2 Summary of seven large compositional mapping sites (see Figure 2 for their locations indicated by white boxes) in the lunar maria and M^3-derived mean TiO_2 abundance of RMDSs in each region.

Region	**Host mare**	**Center coordinate (longitude, latitude)**	**RMDS number**	**Mean TiO_2 abundance (wt%)**
R1	Tranquillitatis	31.493, 10.499	890	5.52
R2	Tranquillitatis	27.948, 5.993	326	5.63
R3	Fecunditatis	55.442, 0.501	263	5.47
R4	Fecunditatis	52.001, -1.500	359	5.38
R5	Nubium	-12.540, -25.469	74	4.95
R6	Humorum	-38.488, -22.953	193	5.08
R7	Procellarum	-43.004, -10.478	302	5.73

Table 3 Mean elemental abundances of the twelve RMDS-specific sites (see also Table 1), obtained using M^3 data (the values are elemental abundances in wt%, oxide abundances).

Area	**Elemental abundances (wt%)**				
	CaO	**Al_2O_3**	**FeO**	**MgO**	**TiO_2**
A1	11.68 +/- 0.42	16.92 +/- 1.23	16.93 +/- 1.08	12.08 +/- 1.25	6.40 +/- 0.23
A2	11.77 +/- 0.41	17.08 +/- 0.76	17.22 +/- 0.62	11.62 +/- 0.88	6.33 +/- 0.23
A3	11.59 +/- 0.43	17.23 +/- 1.00	15.97 +/- 0.77	12.55 +/- 1.18	5.55 +/- 0.35
A4	10.58 +/- 0.83	14.94 +/- 1.93	18.00 +/- 1.52	14.95 +/- 2.12	4.78 +/- 0.27
A5	11.83 +/- 0.46	16.74 +/- 1.08	17.19 +/- 0.96	12.30 +/- 1.32	5.82 +/- 0.80
A6	12.24 +/- 0.41	17.45 +/- 0.93	16.78 +/- 0.80	11.30+/- 1.03	6.27 +/- 0.47
A7	12.12 +/- 0.18	17.42 +/- 0.38	16.83 +/- 0.50	11.33 +/- 0.57	6.25 +/- 0.48
A8	12.14 +/- 0.21	17.30 +/- 0.47	16.79 +/- 0.41	11.62 +/- 0.48	5.82+/- 0.10
A9	10.44 +/- 0.35	14.62 +/- 0.85	18.45 +/- 0.75	14.97 +/- 0.85	5.25 +/- 0.18
A10	11.05 +/- 0.32	15.07 +/- 0.74	19.12+/- 0.59	13.45 +/- 0.82	5.72 +/- 0.17
A11	10.99 +/- 0.32	14.98 +/- 0.77	19.04 +/- 0.67	13.70 +/- 0.83	5.57 +/- 0.15
A12	11.10 +/- 0.25	15.36 +/- 0.51	18.58 +/- 0.64	13.45 +/- 0.62	5.65 +/- 0.37

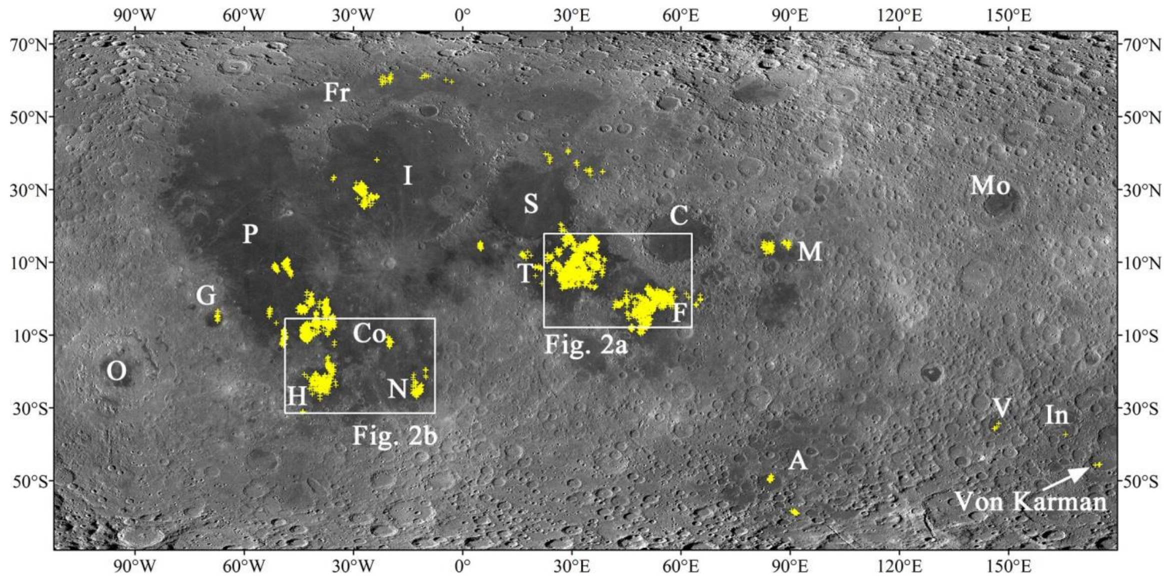

Figure 1. Distribution of more than 8,000 RMDSs (yellow crosses) identified in the lunar maria, updated Figure 2 from Zhang et al. (2017). The two white boxes indicate the locations of enlarged views shown in Figures 2a and 2b, respectively. The basemap is the ~100 m/pixel LROC WAC global morphological mosaic (at 643 nm; Wagner et al., 2015). The Simple Cylindrical projection is used here. Abbreviations: Imbrium (I), Serenitatis (S), Crisium (C), Tranquillitatis (T), Fecunditatis (F), Humorum (H), Nubium (N), Marginis (M), Australe (A), Orientale (O), Grimaldi (G), Frigoris (Fr), Cognitum (Co), Jules Verne (V), Oceanus Procellarum (P), Moscoviense (Mo), Ingenii (In).

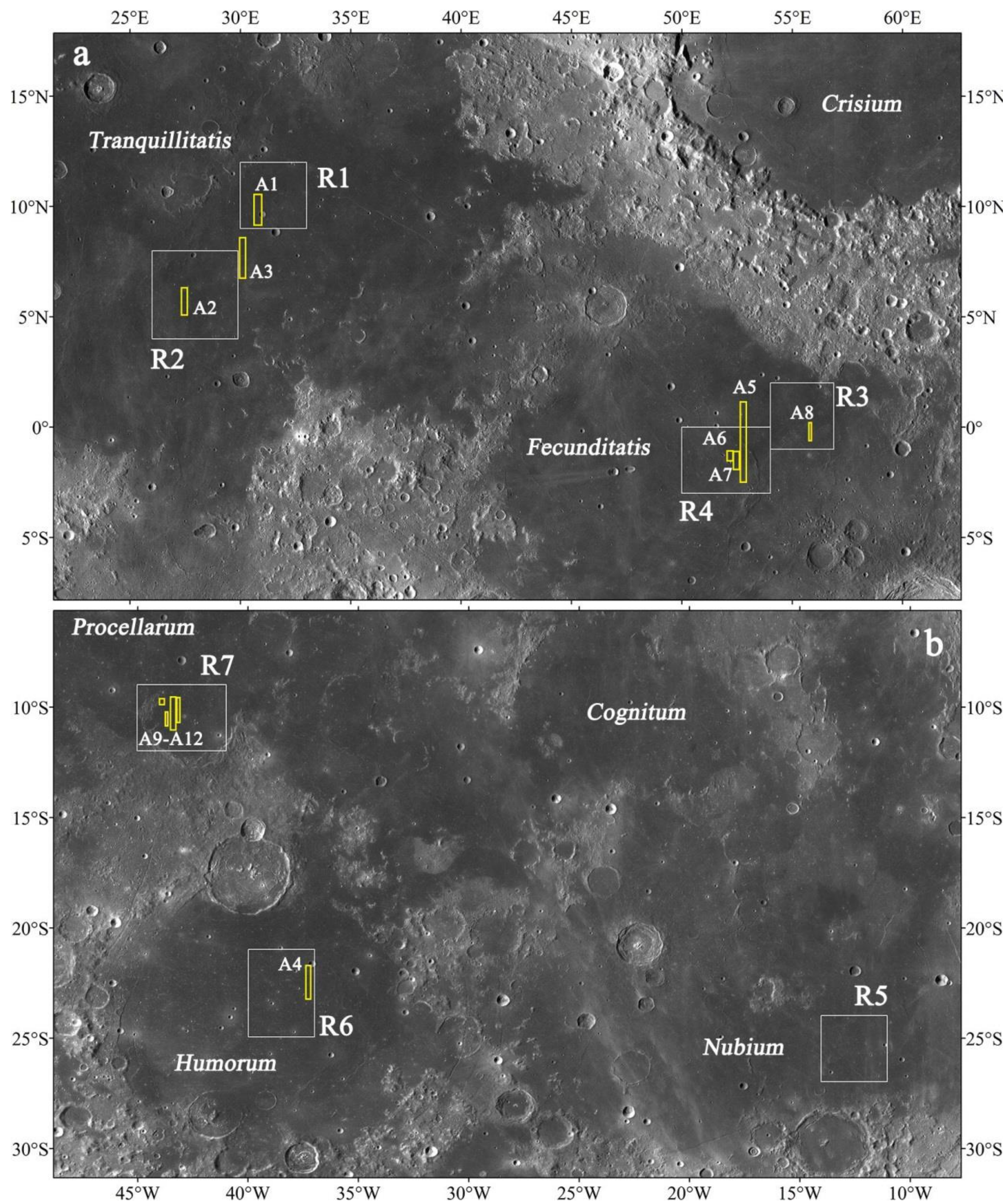

Figure 2. Locations of mare regions showing RMDS-concentrations that are used to perform quantitative measurements of RMDS size (yellow boxes) and compositional mapping of Ti content (white boxes). (a) Locations of mare regions showing RMDS-concentrations in Mare Tranquillitatis and Fecunditatis; (b) Locations of mare regions showing RMDS-concentrations in Mare Nubium, Humorum, and Procellarum. A1-A12 indicate areas 1 to 12 for measuring diameters, heights, and volumes of RMDSs (see Table 1 for detail). R1-R7 represent regions 1 to 7 for performing elemental mapping

of Ti content (see Table 2 for detail).

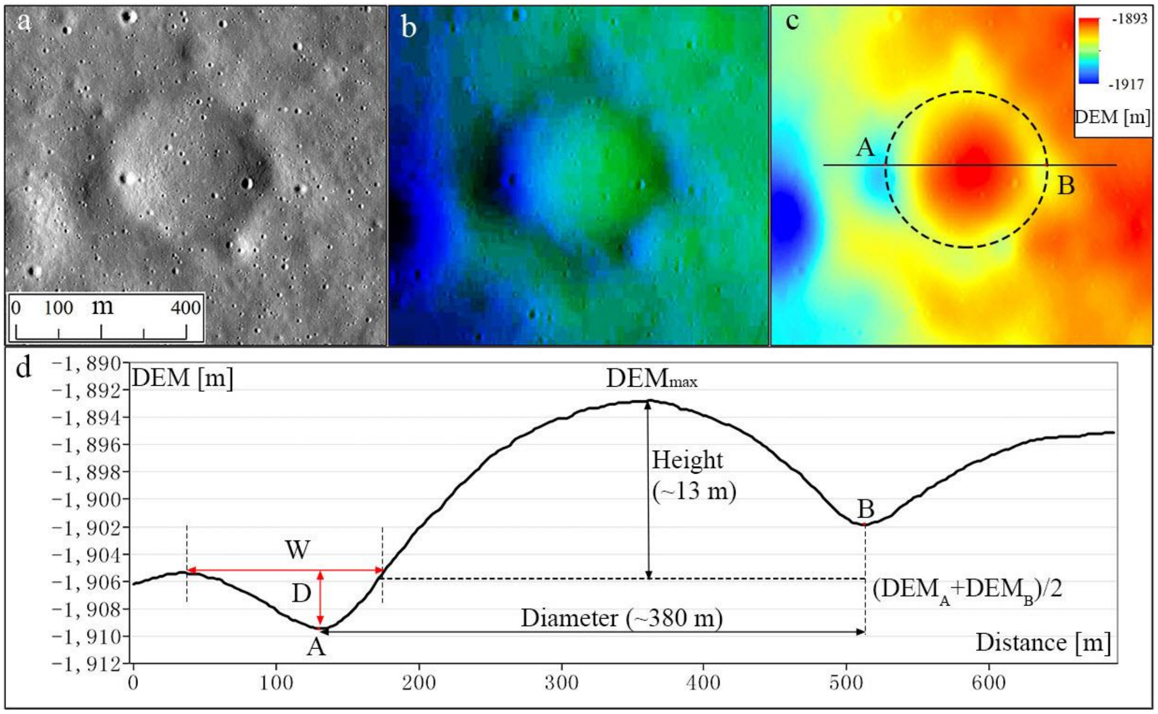

Figure 3. LROC NAC image (a, M1172873803LE) and shaded NAC-based DEMs (b) and colored DEMs (c) for a RMDS example illustrating how to measure the diameter and height of a RMDS, as well as the width (W) and depth (D) of its moat. The topographic profile (d) is extracted along the line indicated in Figure (c), in which the points A and B represent the western and eastern rim (edge) of the RMDS (located in their moat floor, manually marked from the colored, shaded DEM (b)).

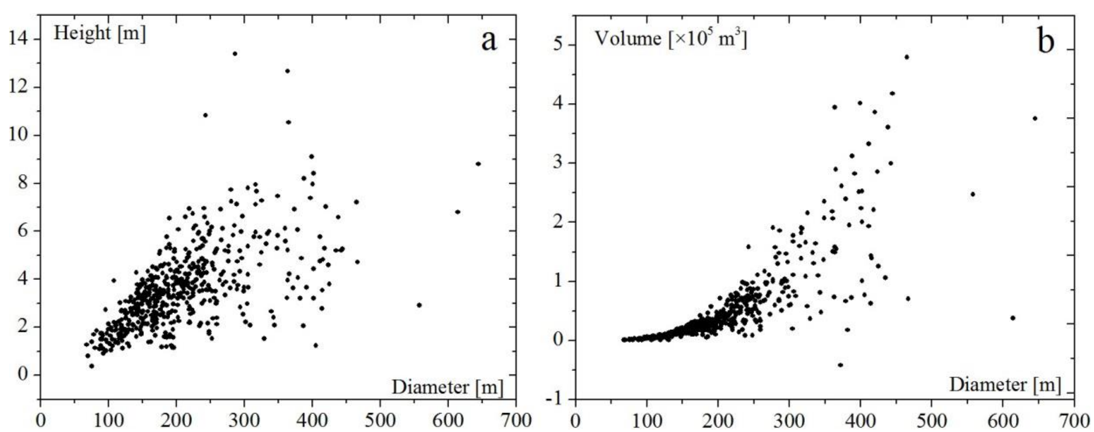

Figure 4. Scatter plots of diameters, heights, and volumes of the 532 RMDSs measured from NAC-derived DTMs: (a) diameter vs. height; (b) diameter vs. volume.

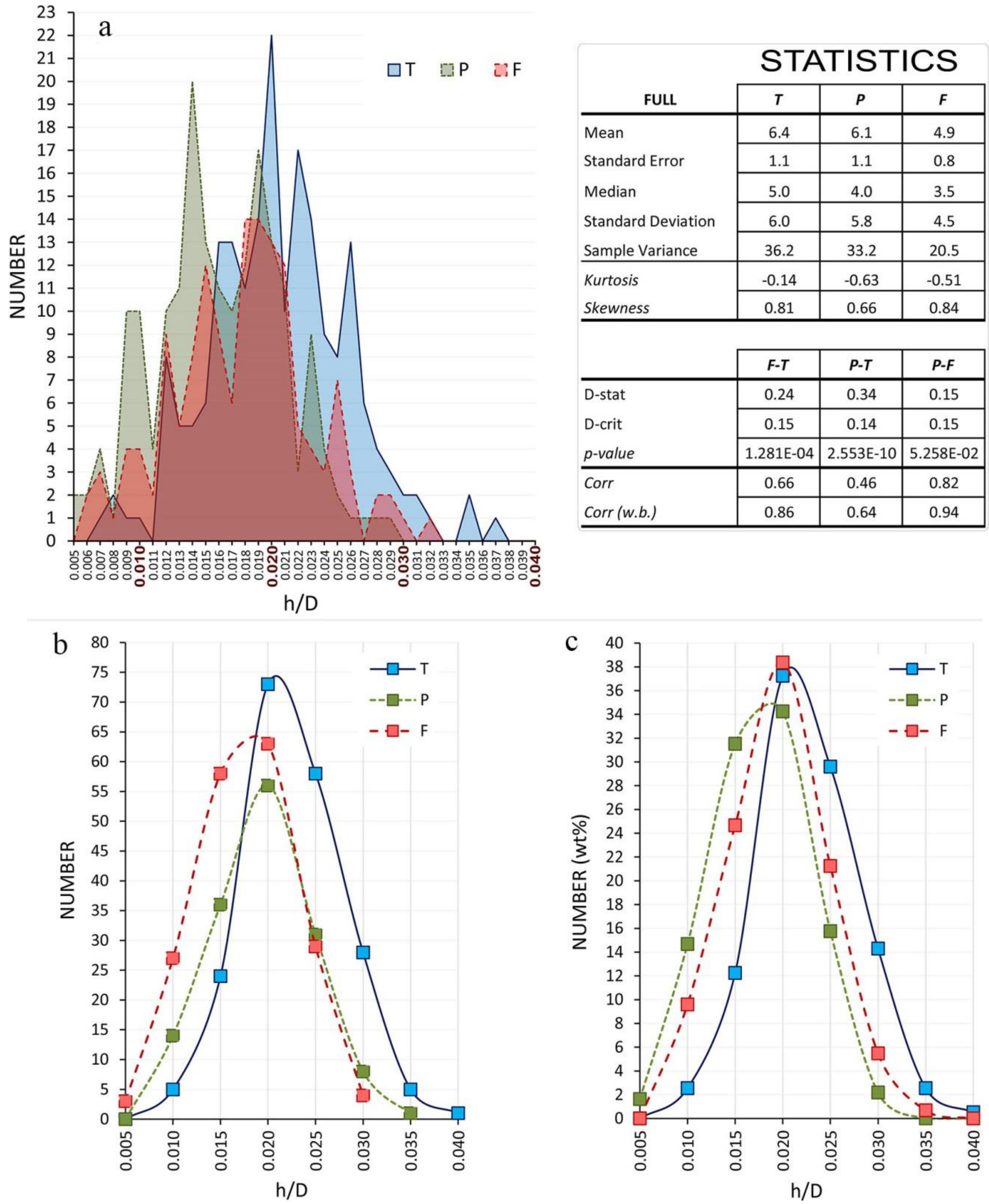

FULL	*T*	*P*	*F*
Mean	6.4	6.1	4.9
Standard Error	1.1	1.1	0.8
Median	5.0	4.0	3.5
Standard Deviation	6.0	5.8	4.5
Sample Variance	36.2	33.2	20.5
Kurtosis	-0.14	-0.63	-0.51
Skewness	0.81	0.66	0.84

	F-T	*P-T*	*P-F*
D-stat	0.24	0.34	0.15
D-crit	0.15	0.14	0.15
p-value	1.281E-04	2.553E-10	5.258E-02
Corr	0.66	0.46	0.82
Corr (w.b.)	0.86	0.64	0.94

Figure 5. Height to Diameter (h/D) histogram plots to compare RMDSs morphologies between the three geologic settings: Tranquillitatis (T), Procellarum (P), and Fecunditatis (F). (a) is a histogram of the distribution of h/D ratios among the RMDSs populations; (b) is equivalent to histogram (a) but with wider bin sizes (from the original 0.001 to 0.005): this smoothens the distribution to aid interpretation. (c) represents the same data but

normalised to 100, i.e., percentage (%), which highlights the relative distribution of h/D regardless of the variations in sample sizes among the regions. The statistics table compares distributions for the individual regions (upper part) and statistical correlations between settings (lower part).

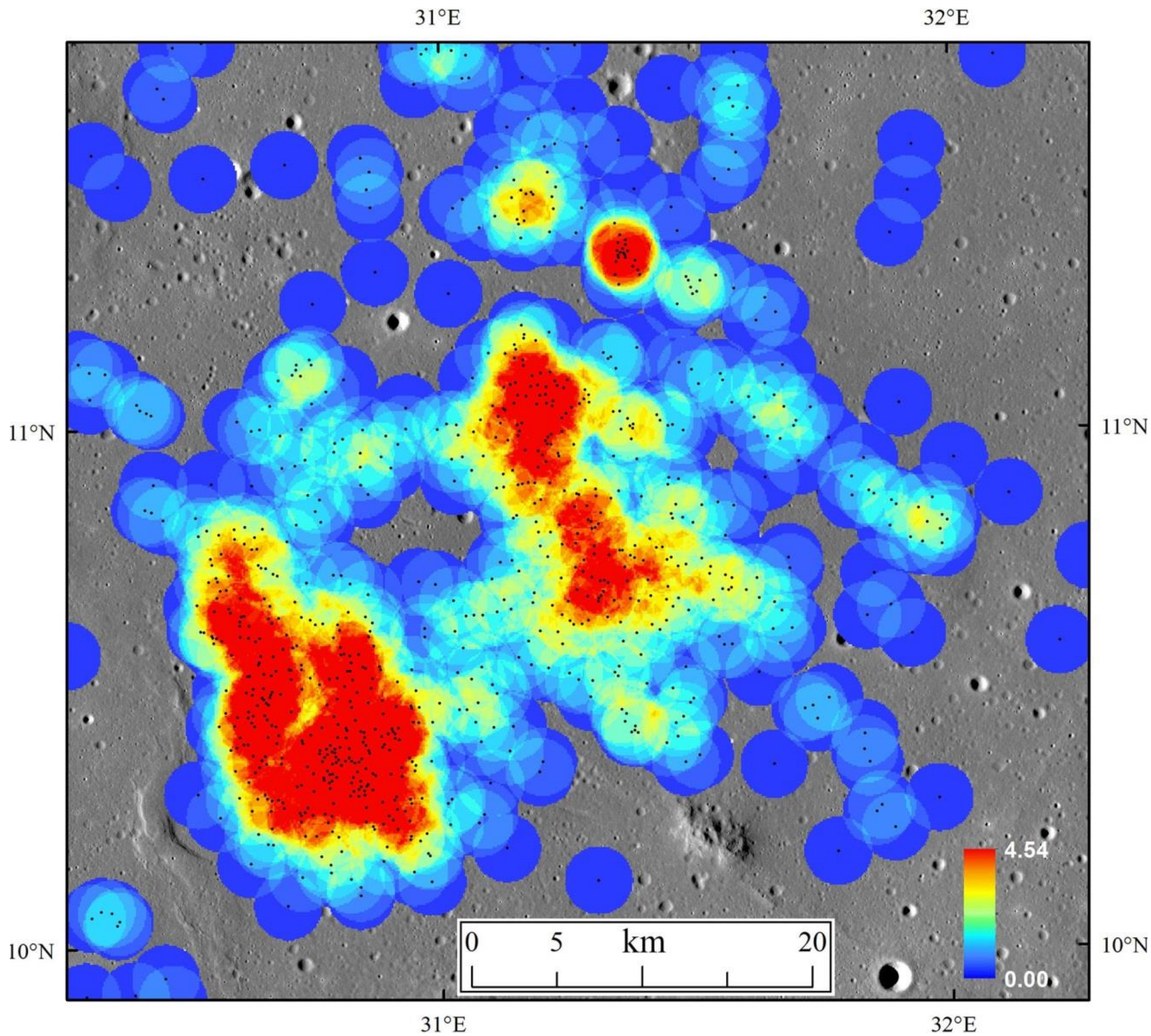

Figure 6. Point density map of 870 RMDSs (black dots) in central Mare Tranquillitatis (same region as indicated in Figure 1a from Zhang et al. (2017), R1 in Figure 2a and also see Figure 14 for more detail). The basemap is Kaguya TC mosaic with a resolution of ~10 m/pixel. Red color represents a high density of RMDSs. The maximum number density of RMDSs is ~5/km^2 with a search radius of 2 km. North is up.

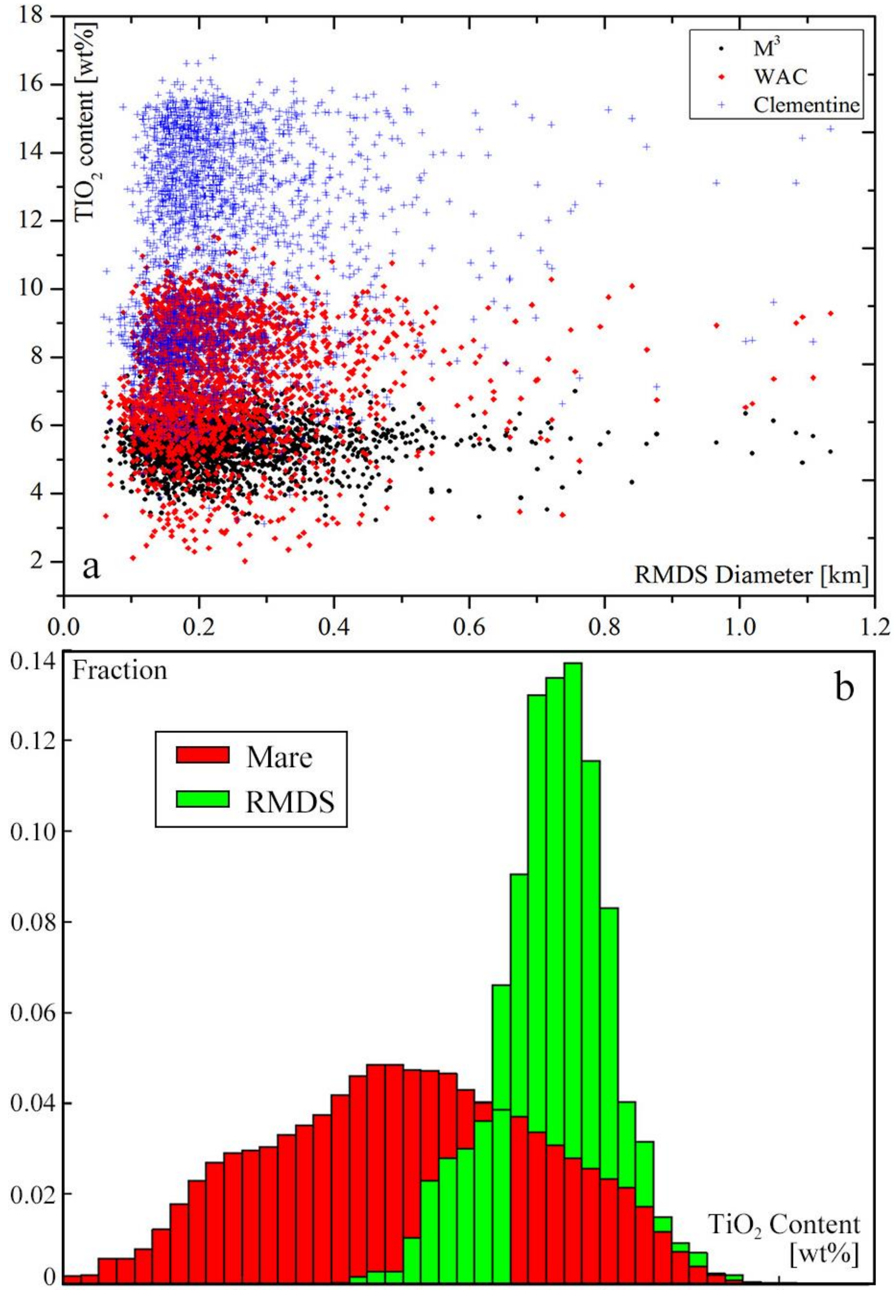

Figure 7. Spectra-derived TiO_2 contents of RMDSs and global maria (latitude range +/- 75 degrees). (a) Mean TiO_2 wt% vs. diameter for 2407 RMDSs in seven large mare regions indicated in Figure 2. Black dots, red diamonds, and blue crosses respectively represent M^3, LRO-WAC, and Clementine-derived TiO_2 contents; (b) The M^3-derived TiO_2 content histogram of the measured 2407 RMDSs (green color), compared with the global TiO_2 distribution of all lunar mare regions (red color). Both histograms are normalized to 1, such that the sum of all red or green histogram bins is 1, respectively.

The global Ti abundance was taken from the complete lunar mare surface at a latitude range +/- 75 degrees.

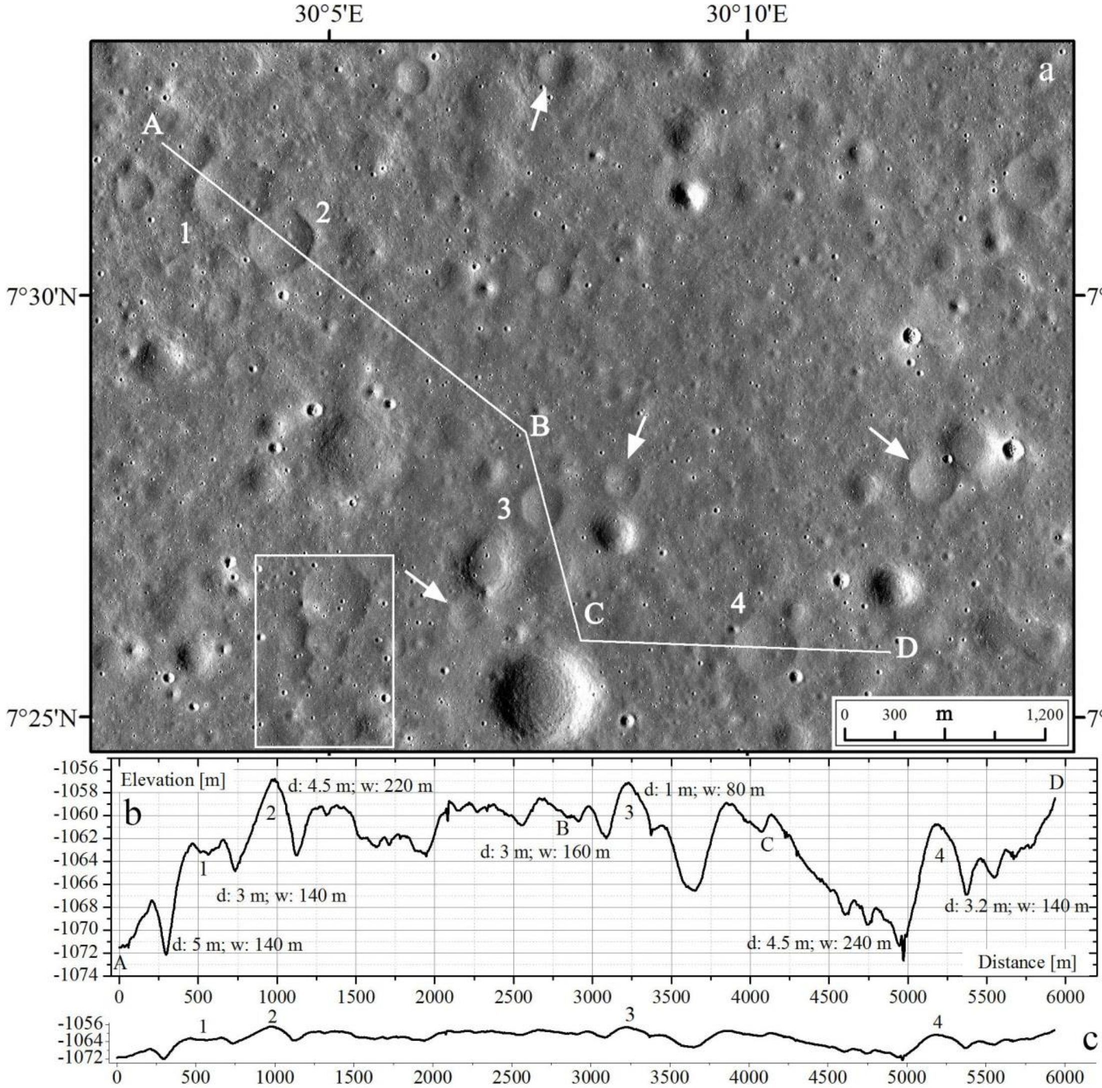

Figure 8. Topographic measurement of the depth (d) and width (w) of the moat of RMDSs. (a) LROC NAC mosaic (M1111613936LE and RE) of a RMDS area in the region 2 (R2, Figure 2a) within Mare Tranquillitatis. White arrows point to RMDSs adjacent to impact craters. A RMDS-chain pattern is outlined by the white box. Numbers 1 to 4 mark the four RMDSs cut through by the broken line AB_BC_CD; (b) NAC-based DEM profile (~70× vertical exaggeration) along the broken line AB_BC_CD indicated in Figure (a); The bottom plot (c) shows a less vertically exaggerated profile (14× vertical exaggeration). The symmetric and asymmetric profiles of the four RMDSs are clearly visible. The depths and widths of their ring moats are measured and labeled in the upper

diagram (b).

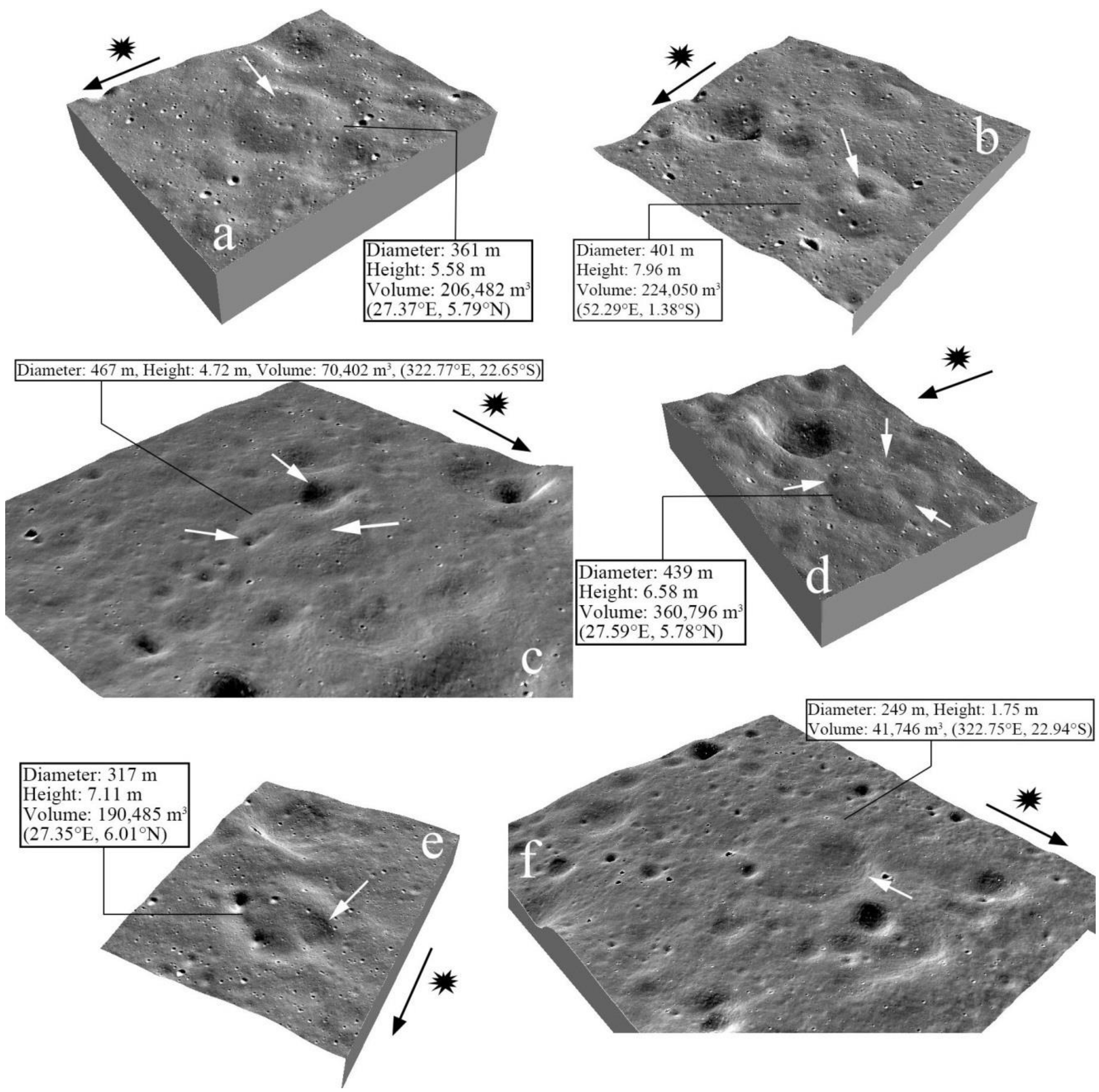

Figure 9. 3D views of RMDSs exhibiting depressions/collapses at their summit, off the center, and in the moat lows, using NACs (frames M1172873803LE and RE, M1142680981LE and RE, M1142098334LE and RE) draped over NAC-based DEMs (2 m/pixel, 6× vertical exaggeration). White arrows indicate depressions/collapses occurring at different RMDS sections. The black arrow in each image illustrates sun illumination direction.

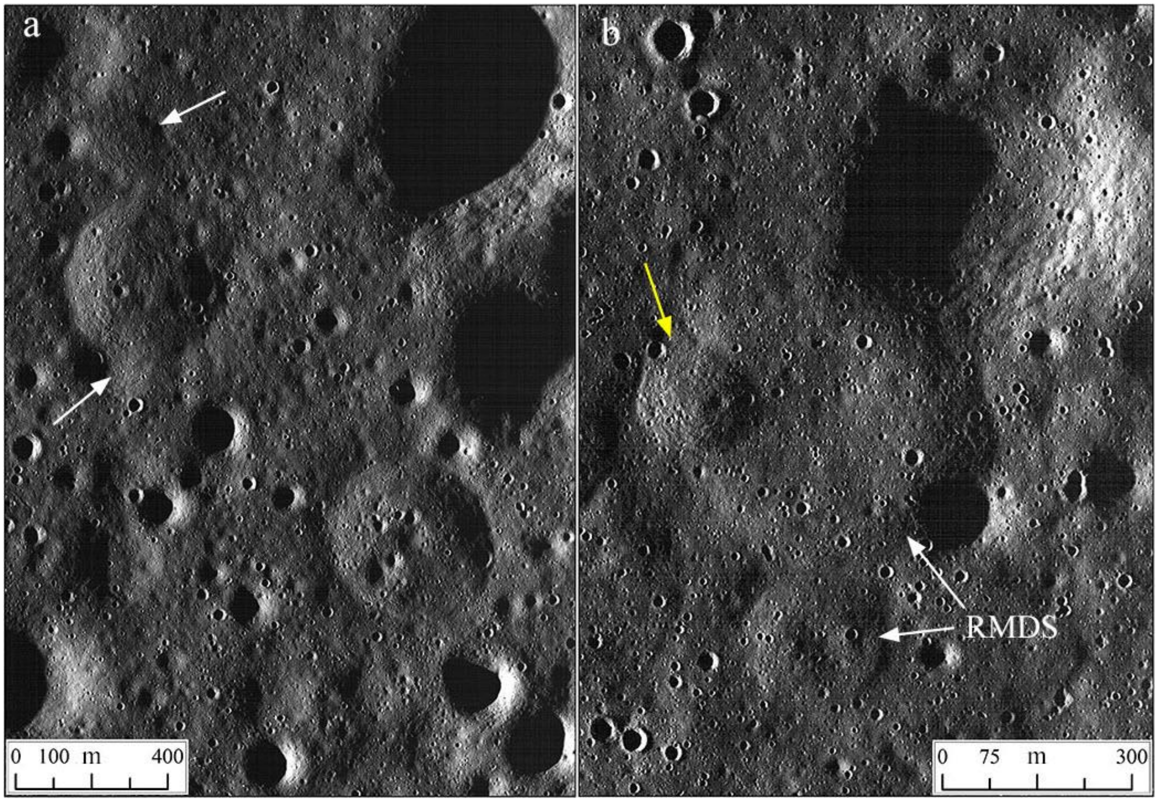

Figure 10. Morphology variation of RMDS areas seen from low-illumination NAC images (The sun illumination direction is from left to right). (a) NAC Frame M117168690RE, feature located at 4.35°S, 49.45°E within Mare Fecunditatis. Two white arrows indicate the parts where the moat appear to be filled by mare or RMDS mound material and connected to the surrounding surface. (b) NAC Frame M117155214RE, feature located at 1.33°N, 51.60°E within Mare Fecunditatis. White arrows show two different sizes of RMDSs that are next to each other. The yellow arrow exhibits a small-size RMDS situated on the western flank of the large RMDS. North is up in all images.

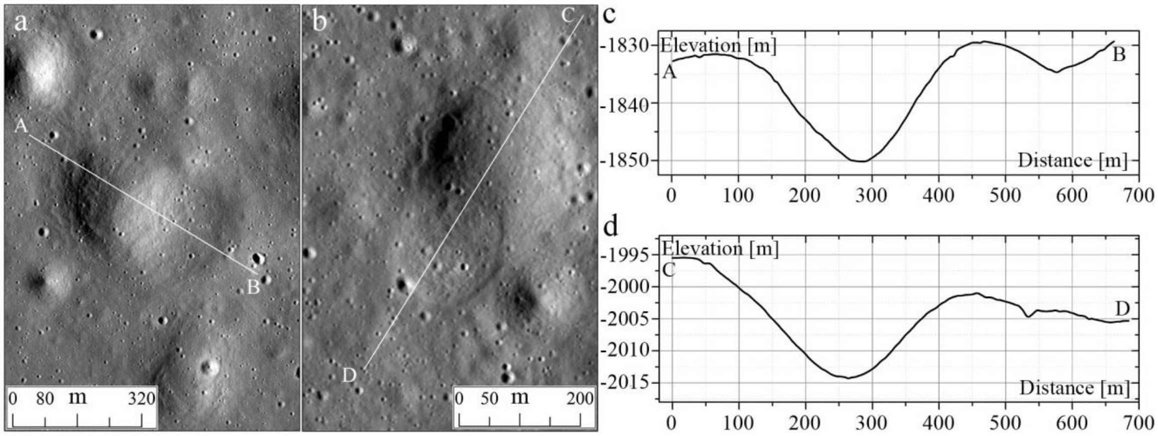

Figure 11. Symmetric profile of the crater cavity partially superposed by RMDS. NAC images for (a) a RMDS in Mare Tranquillitatis (M1172873803LE) and (b) a RMDS in Mare Fecunditatis (M1126787189LE); (c) and (d) are NAC-derived topographic profiles of the RMDS-crater along the transects AB and CD in Figures (a) and (b), respectively.

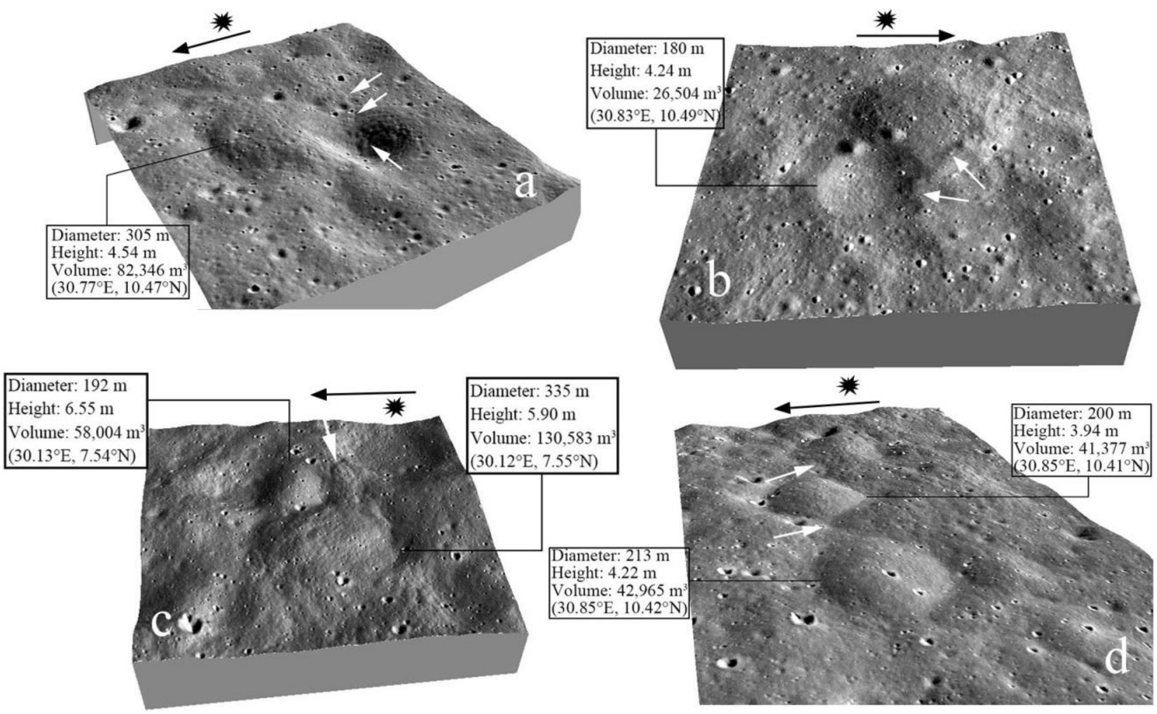

Figure 12. Flow features associated with or surrounding RMDSs (NAC images draped on NAC-DEMs, 6× vertical exaggeration). White arrows in Figures (a), (b), and (d) point to possible lava flow fronts, while the white arrow in Figure (c) shows a lava lobe originating from the 335-diameter RMDS nearby. NAC frame pairs M1096293859 and

M1111613936 are used. The black arrow in each image illustrates the sun illumination direction.

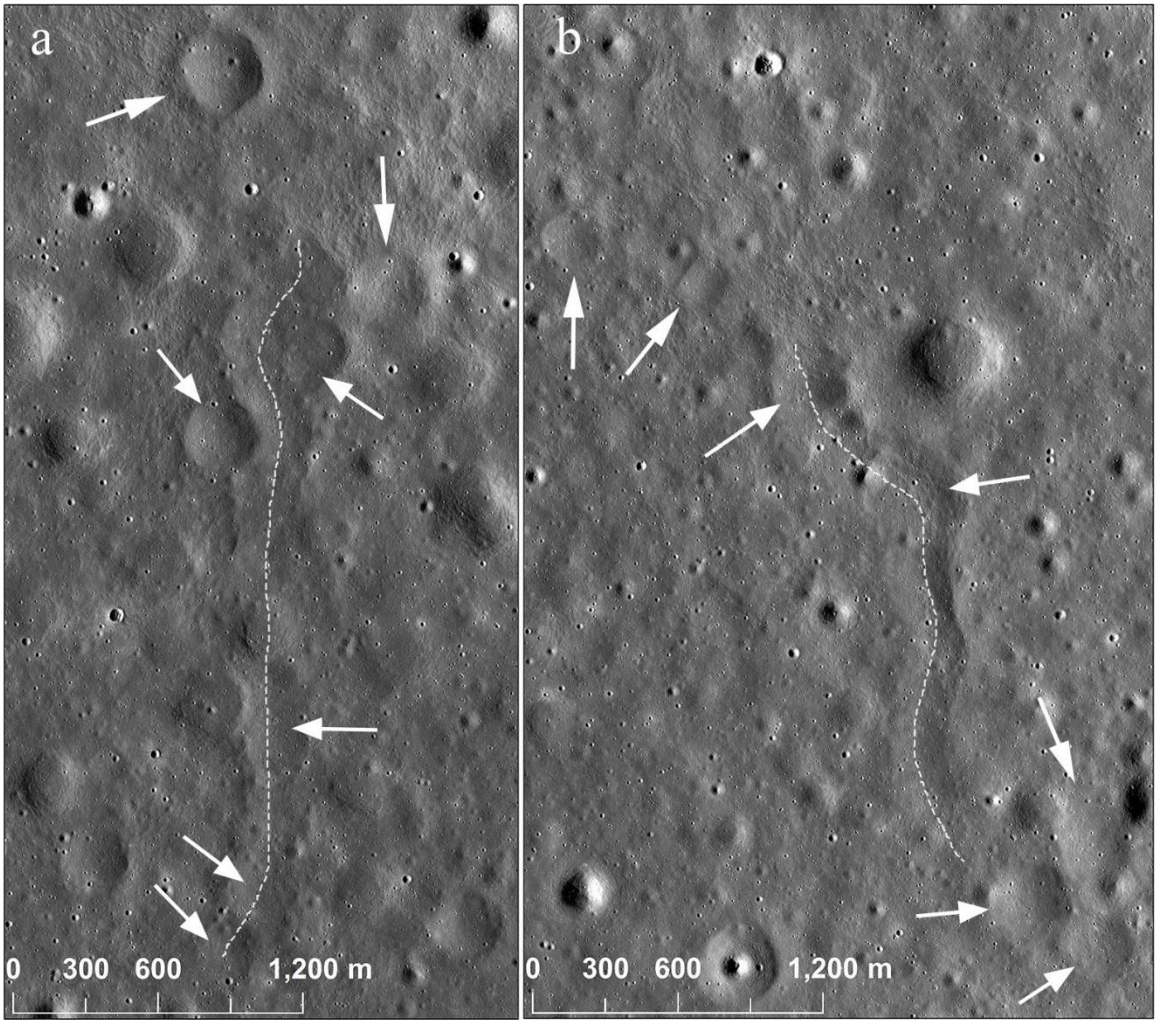

Figure 13. LROC NAC images showing the coexistence of RMDSs and flow lineaments (dashed white lines). (a) RMDSs (white arrows) on or around the linear positive flow feature in northern Mare Tranquillitatis; (b) RMDSs (white arrows) aligned along the extension of a sinuous ridge-like flow feature to the near east of the region in Figure (a). NAC frames M150294225LE and RE are used. The sun illumination direction is from left to right. North is up in all images.

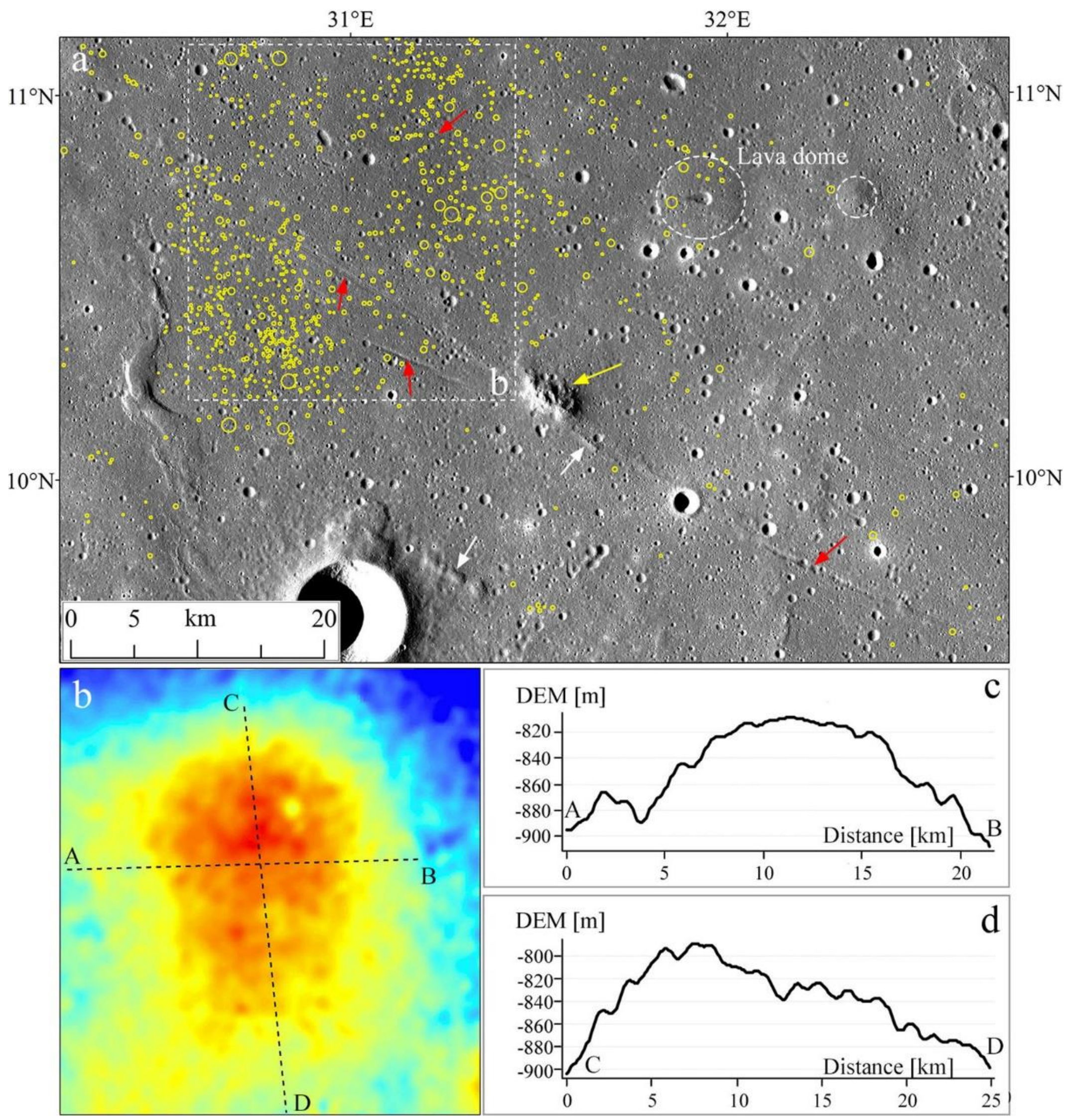

Figure 14. RMDSs and their association with mare domes and linear volcanic features. (a) Kaguya TC mosaic showing two mare domes (Lena et al., 2013) and some linear volcanic features in the RMDS-scattered area located in central Mare Tranquillitatis (R1, Figure 2a). Red and white arrows, respectively, point to extensional lineaments and ridge-like features, while white dashed lines illustrate two mare lava domes. The yellow arrow points to a linear positive structure that was in this study interpreted as a volcanic edifice (probable a volcanic cone). RMDSs are marked by yellow circles; (b) GLD100 DEM color map for a possible large lava dome (~25×20 km in size), indicated by the white box in Figure (a); (c) and (d) are topographic profiles extracted along the dashed lines AB and CD drawn in Figure (b).

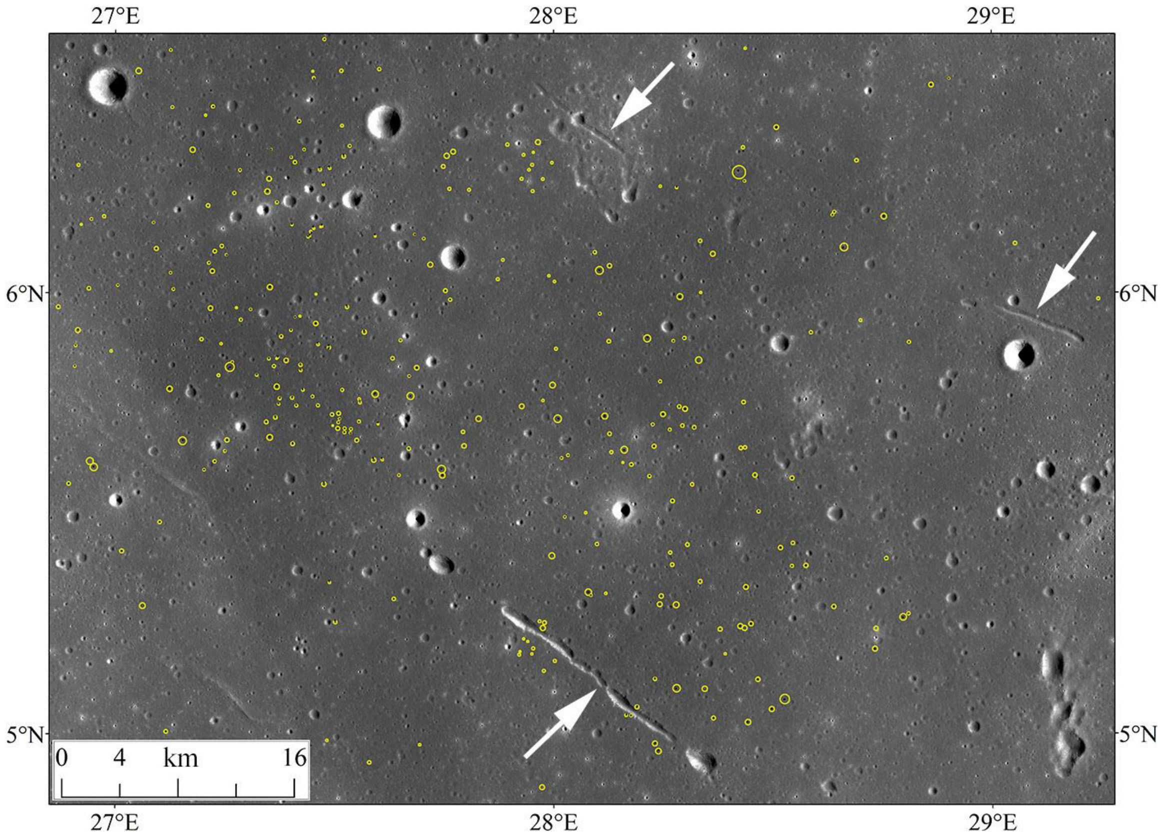

Figure 15. Kaguya TC mosaic for linear negative-relief features (white arrows) in southern Mare Tranquillitatis containing RMDS area 2 indicated in Figure 2a. RMDSs are marked by yellow circles.

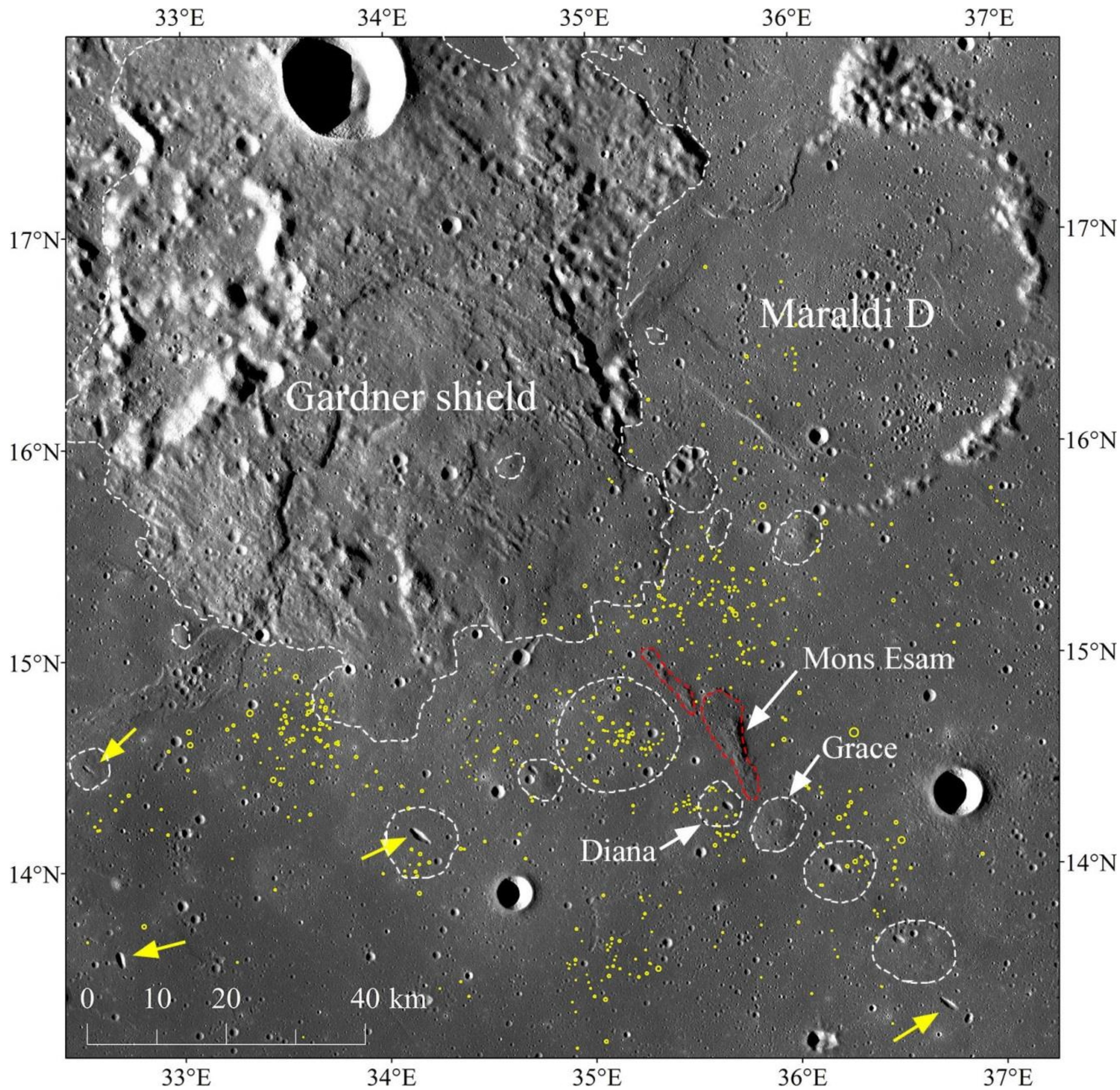

Figure 16. Kaguya TC mosaic for the volcanic features and surrounding RMDSs (yellow circles) in northern Mare Tranquillitatis. White dashed lines indicate volcanic shields and mare domes (Wilhelms, 1972; Zhang et al., 2018b). Red dashed lines mark the cones of Mons Esam (Weitz & Head, 1999). Yellow arrows point to elongate depressions oriented in a NW-SE direction.

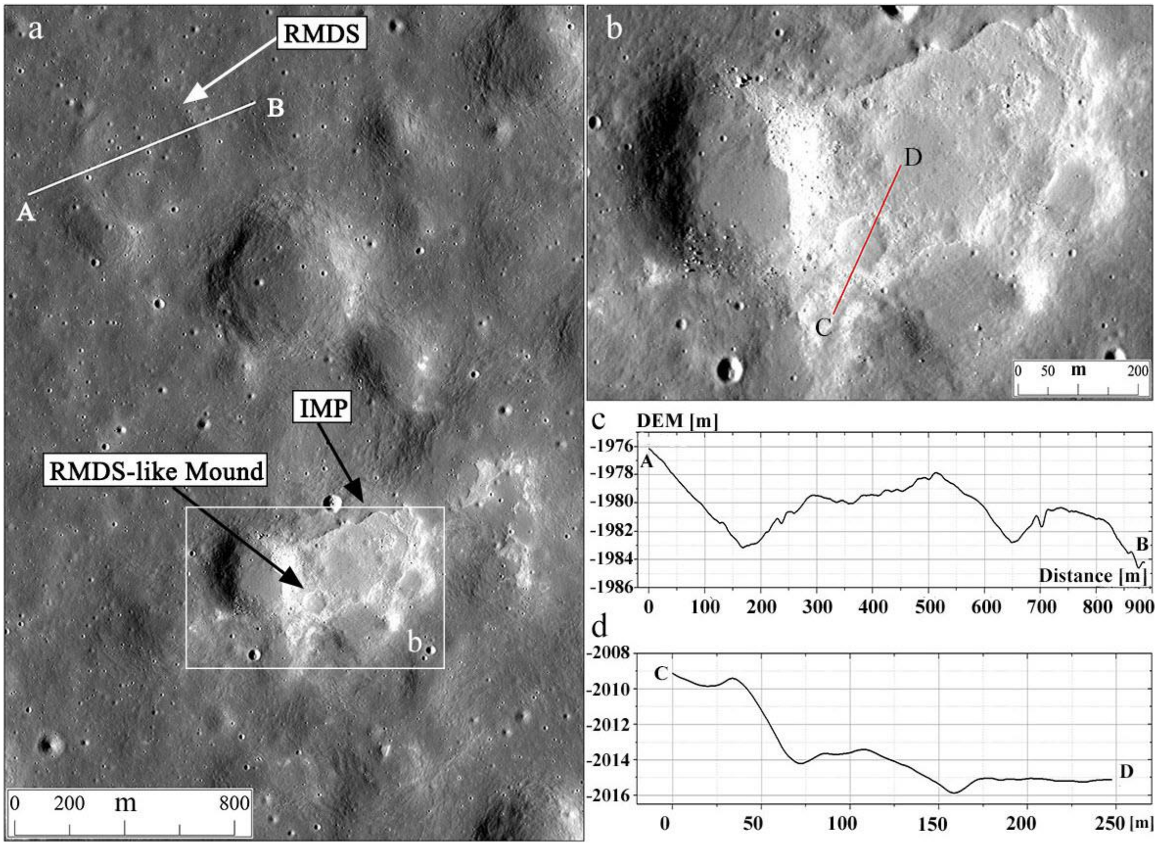

Figure 17. Morphological comparison between a RMDS and a RMDS-like mound inside an IMP in western Mare Tranquillitatis. (a) The RMDS and IMP are shown in NAC image M1111670765RE (Image center location: 21.59°E, 8.32°N); (b) Enlarged view of the RMDS-like mound in the IMP; (c) Topographic profile along the transect AB across the RMDS indicated in Figure (a); (d) Topographic profile along the transect CD across the RMDS-like mound inside the IMP marked in Figure (b). The NAC-based DEM was used to extract the topographic profiles. North is up in all images.

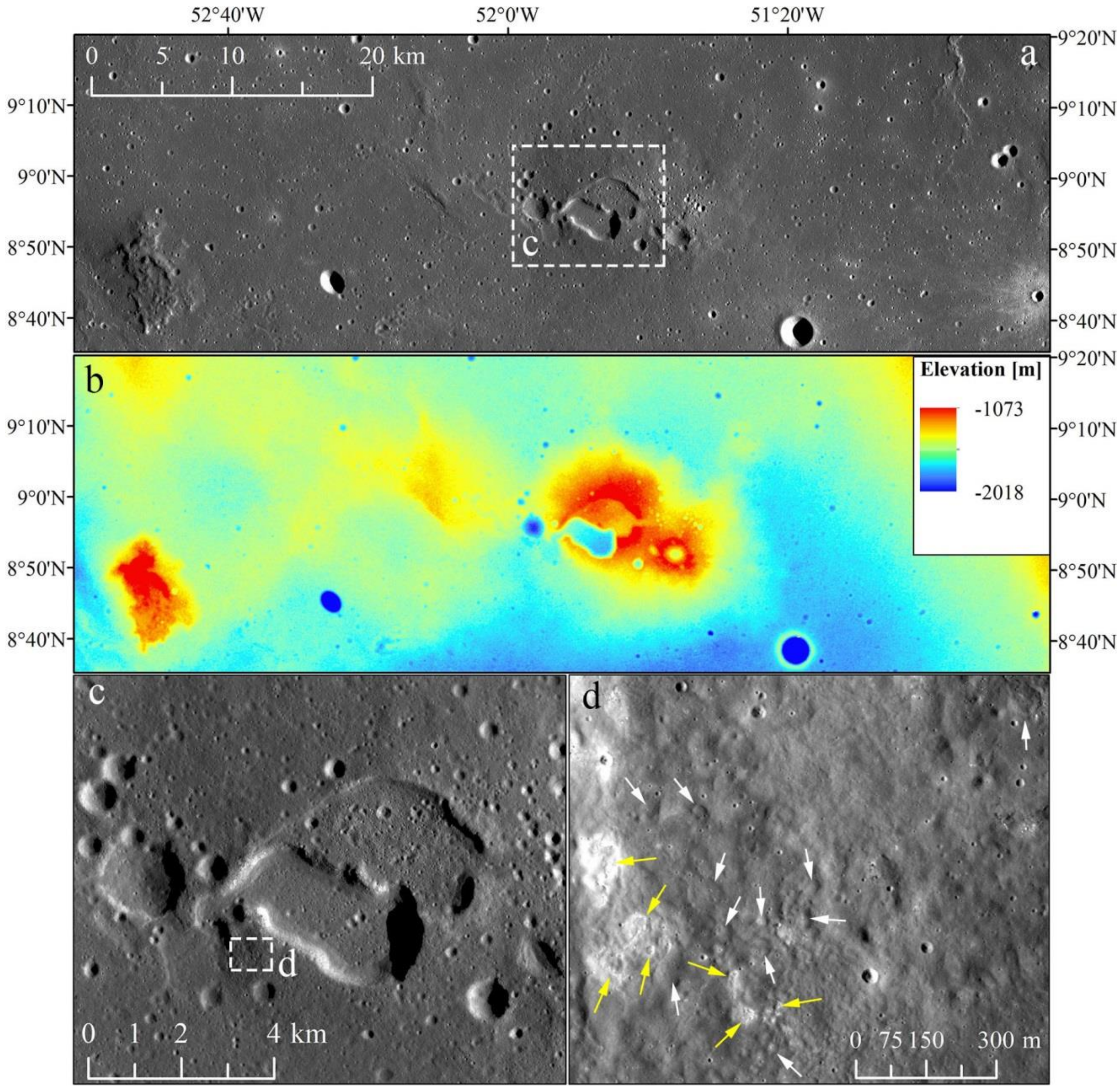

Figure 18. Kaguya TC map and LROC NAC image for the distribution of IMPs, with neighboring RMDSs, at the boundary of a volcanic vent in Procellarum. (a) Kaguya TC morning map and (b) Kaguya TC-derived DEM for the geologic setting of the volcanic edifice with summit pit craters oriented in west-to-east direction; (c) The enlarged view of the volcanic vents indicated by the dashed white box in Figure (a). The dashed white box in Figure (c) illustrates the place of the concurrent occurrence of IMPs and RMDSs as shown in Figure (d); (d) NAC image (frame M181509373LE) for the detail of IMP-RMDS association. White arrows indicate RMDS-like mounds, while yellow arrows point to IMPs.

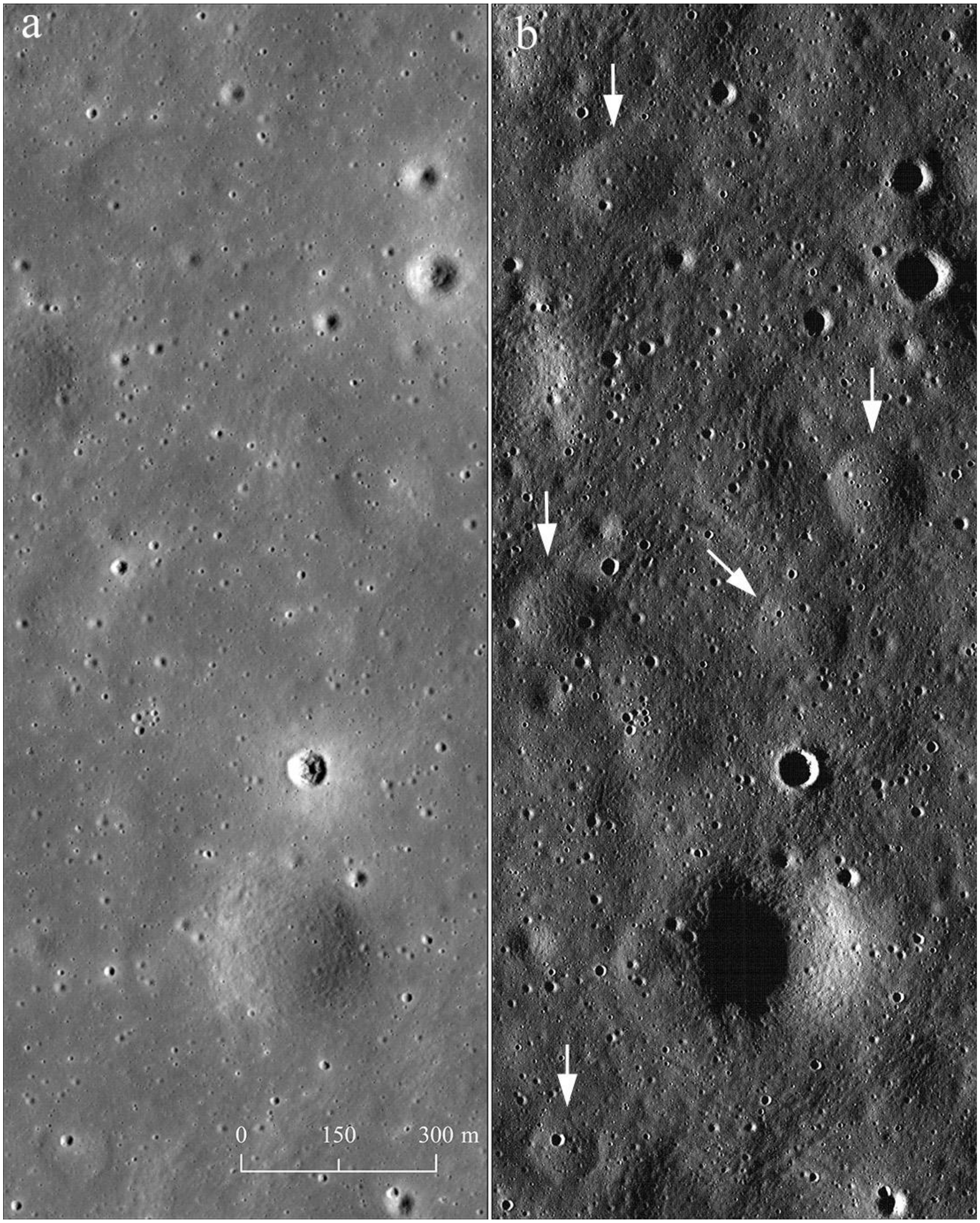

Figure 19. Images of the same area showing RMDS occurrences (located in Mare Tranquillitatis) in normal image solar illumination geometry (a, NAC frame: M1108067963LE; Incidence angle: 64.19) and in lower solar illumination geometry image (b, NAC frame: M117277488RE; Incidence angle: 84.23). The sun illumination direction is (a) from right to left, but (b) from left to right. White arrows in (b) point to RMDSs. North is up in both images.